An Exploration of Theoretical Spectra

Lauren N. Koulias

A dissertation
submitted in partial fulfillment of the
requirements for the degree of

Doctor of Philosophy

University of Washington

2023

Reading Committee:
Xiaosong Li, Chair
Stefan Stoll
Brandi Cossairt

Program Authorized to Offer Degree:
Chemistry

University of Washington

Abstract

An Exploration of Theoretical Spectra

Lauren N. Koulias

Chair of the Supervisory Committee:
Xiaosong Li
Department of Chemistry

This thesis presents an exploration of theoretical spectra, both in their creation and interpretation, with a focus on coupled cluster methods and an emphasis on the importance of relativistic effects. Throughout this work the X2C Hamiltonian is utilized to produce the reference wavefunction, including both scalar relativistic effects and spin-orbit coupling variationally in the presented schemes.

First, a relativistic equation-of-motion coupled-cluster with single and double excitations (X2C-EOM-CCSD) formalism is presented including a discussion of the massively parallelized implementation available in the ChronusQuatum software package. In order to evaluate the accuracy of X2C-EOM-CCSD, we compare calculated, experimental, and TDDFT results, looking at zero-field splitting values. In addition to calculating the excitation energies for this low energy region, the oscillator strength of each excitation is calculated. This enables the simulation of absorption spectra, the observation of which excited states are populated, and the comparison of other general spectral features in the low energy UV-Visible region in order to benchmark the accuracy.

Additionally, a relativistic time-dependent equation-of-motion coupled-cluster with single and double excitations (TD-EOM-CCSD) formalism is presented. Unlike other explicitly time-dependent quantum chemical methods, the present approach considers the time correlation function of the dipole operator, as opposed to the expectation value of the time-

dependent dipole moment. The accuracy of X2C-TD-EOM-CCSD is evaluated by comparing zero-field splitting in atomic absorption spectra of open-shell systems (Na, K, Mg^+, and Ca^+) with values obtained from experiment. In closed-shell species (Na^+, K^+, Mg^{2+}, and Ca^{2+}), singlet triplet mixing is observed in the X2C-TD-EOM-CC calculations, which results from the use of the X2C reference. The effects of the X2C reference are evaluated by comparing spectra derived from X2C-TD-EOM-CC calculations to those from TD-EOM-CC calculations using a complex generalized Hartree-Fock ($\mathbb{C}$-GHF) reference.

The interpretation of spectra is an arduous task that can be simplified with the use of spectral analysis tools. The Python library, **fasma**, is presented as a tool to help simplify this problem. By breaking down spectra into angular momentum character or molecular orbital contributions, along with giving information about the excitation order of each transition, various regions of the spectra can be interpreted and features of interest can be quickly identified. While keeping ease of use in mind, this library also allows extensive customization of analysis by the user through the quantity of information from electronic structure calculations that is made into easily accessible Python objects.

TABLE OF CONTENTS

LIST OF FIGURES

LIST OF TABLES

ABBREVIATIONS

CAS: complete active space

CCSD: coupled cluster singles and doubles

CI: configuration interaction

EOM: equation of motion

LR: linear response

MO: molecular orbitals

OS: oscillator strength

PDM: one particle density matrix

SCF: self consistent field

TDDFT: time-dependent density functional theory

TDHF: time-dependent hartree-fock

X2C: exact two component

XAS: x-ray absorption spectroscopy

4C: four component

Dedicated to those who appreciate the terrors of grad school and all of the wonderful teachers who inspired me.

ACKNOWLEDGMENTS

There are so many people that I need to thank for supporting me in getting to where I am today. Of course I need to thank my parents, for supporting my curiosity at an early age and never limiting my potential.

And then there is my wonderful husband Justin, who has been by my side throughout the last six years. I don't know how I would have survived moving to the farthest possible corner of the continental U.S. without you. God knows neither of us would have lasted out here without the other. I love you and I'm sorry I dragged you into this with me. Hopefully you'll forgive me for that one day.

Throughout my life there have been many wonderful teachers that inspired me and I want to thank each and every one of the, but especially the Priddys who started it all. Without the Priddys, my two favorite high school teachers, I would never have been inspired to pursue a career in science or education. Looking back, they prove how influential and important good teachers are and I will never forget learning how to gamble after the AP stats exam or extracting the DNA from strawberries in chem club.

I also need to thank Prof. A. Eugene Deprince III for allowing me to do undergraduate research in his lab and helping me decide to go to grad school. Oh, and also for that copy of Adam Ruben's "Surviving Your Stupid, Stupid Decision to Go to Grad School" that has been sitting on my bookshelf for the last six years.

Then of course there is my advisor, Prof. Xiaosong Li, who has supported me throughout the ups and downs of grad school. Thank you for supporting me in pursuing my interests and for letting me TA even when it wasn't the most convenient.

This brings me to thanking Prof. Gary Drobny for letting me expand my teaching skills

with his wonderful PChem students. They've really been one of the highlights of my last two years and confirmed my love of teaching, even though they only occasionally showed interest in my derivations.

Finally, I need to thank all of the friends I have made here at UW and the older grad students and postdocs who have mentored me. You guys made this grey city tolerable.

Chapter 1

RELATIVISTIC EQUATION OF MOTION COUPLED CLUSTER

This chapter has been adapted from work done by Lauren N. Koulias in collaboration with Tianyuan Zhang, Lixin Lu, Edward F. Valeev, A. Eugene DePrince III, and Xiaosong Li. It is currently in the pre-submission stage of publication.

1.1 Introduction

Excited state methods that are based off the coupled-cluster (CC) theory[18, 111, 34, 110] can provide accurate descriptions of spectroscopic features, such as excitation frequencies and oscillator strengths, and are rigorously size extensive when truncated at any excitation order. These methods include the linear response CC (LR–CC)[73, 19, 52, 51, 53], the equation-of-motion CC (EOM–CC)[75, 29, 110], and the symmetry adapted cluster configuration interaction (SAC-CI)[76] formalisms. While these methods in the non-relativistic regime are widely used and highly accurate for describing valence electron excitations of light elements, the inclusion of relativistic effects into calculations is important when dealing with core level spectroscopy, valence electron excitations of heavy elements, and spin-forbidden processes.

Relativistic effects, including scalar and spin-orbit effects, are known to cause orbital contraction, increase in binding energy, mix spin states, modify hybridization in the valence shell, spectral splitting, and inter-system crossing.[92, 93, 70, 119] The X2C approach is a popular variational approach to incorporate relativistic effects. It has been shown to be an accurate approach to describe the spin-orbit splittings of both valence and core electrons[124, 35, 27, 28, 89, 48]. Within the CC framework, perturbative treatments of spin-orbit couplings have been used for LR- and EOM-CC calculations.[15, 30, 50, 16, 12, 127, 117, 122] Recently,

relativistic EOM-CC methods in which spin-orbit couplings are included variationally at the molecular orbital level have been introduced and show excellent accuracy in the description of excitation energies and fine-structure splitting.[5, 107, 3, 63, 82, 55]

In this work, we report an implementation of a Kramers-unrestricted form of EOM-CC with single and double excitations (EOM-CCSD) within the relativistic two-component framework. In addition to excitation energies, expressions for computing oscillator strengths are also presented in this paper. Both scalar and spin-orbit relativistic effects are included variationally at the reference level. Benchmark tests focus on simulated atomic and molecular absorption spectra in the UV/Vis regime and excited state fine-structure splitting, as well as applications to lifetime prediction and the calculation of spectroscopic constants.

1.2 Theory

1.2.1 Kramers-Unrestricted Two-Component Reference Wave Function

We have formulated our relativistic EOM-CC approach for the Kramers-unrestricted case, which, for open-shell systems, can lead to the breaking of time-reversal symmetry[60]. The spinor molecular orbitals from a relativistic two-component reference are used in the relativistic EOM-CCSD method. Here, a brief summary of this relativistic two-component approach is presented. For a more thorough review, please refer to Refs. 26, 96, 65.

All two-component methods start from the same place: the four-component Dirac equation. The large and small components of this equation are decoupled via a unitary transformation $\mathcal{U}$, yielding a block diagonalized four-component Hamiltonian:

$$\mathcal{U}^\dagger \hat{\mathcal{H}} \mathcal{U} = \begin{pmatrix} \mathbb{H}^+ & \mathbf{0}_2 \\ \mathbf{0}_2 & \mathbb{H}^- \end{pmatrix} \tag{1.1}$$

where $\mathbb{H}^+$ are the electronic solutions and $\mathbb{H}^-$ are the negative energy solutions, which can be disregarded. As a result only $\mathbb{H}^+$, which is the two-component Hamiltonian corresponding to the electronic solutions, needs be computed.

When looking at the wave function, this unitary transformation, $\mathcal{U}$, effectively "folds" the small component into the large component, eliminating the need for the small component to be evaluated:

$$\mathcal{U}\begin{pmatrix}\psi_L\\ \psi_S\end{pmatrix} = \begin{pmatrix}\tilde{\psi}_L\\ 0\end{pmatrix} \tag{1.2}$$

Here, the X2C transformation [57, 66, 85, 44, 67, 64, 102, 62, 86, 27, 35, 54, 28, 89, 68] is used for $\mathcal{U}$. The decoupling scheme in this approach is obtained by solving the one-body Dirac-Hartree-Fock equation, where the bare Coulomb operator is used for the two-electron term. Neglecting to transform the two-electron Coulomb repulsion operator is the leading cause of error in the X2C transformation. This error is compensated for using the Boettger factor[9], an empirical correction which scales the one-electron spin orbit terms to approximately account for the two-electron spin-orbit interactions.

Due to this one-electron X2C framework, the transformation (or "picture change" as it is commonly referred to) is independent of the two-electron operator. Since the transformation from four- to two-component depends only on the basis set used in the one-electron Hamiltonian, the picture change error needs not be considered in post-SCF methods. This simplification is the main advantage of using an effective one-electron X2C approach in this context[45].

1.2.2 Two-Component Equation-of-Motion Coupled-Cluster

Throughout this Section, the labels *i,j,k,l,m,n* refer to molecular orbitals (MOs) that are occupied in the reference configuration, while *a,b,c,d,e,f* refer to MOs that are unoccupied. Due to the structure of the relativistic components of the Hamiltonian, the EOM-CC equations must be formulated with complex arithmetic and spin-broken amplitudes. As compared to non-relativistic EOM-CC calculations, these properties increase the storage requirements and the number of floating point operations, but the formal scaling properties of EOM-CC

remain unchanged.

The ground-state CC with single and double excitations (CCSD) wave function is given by $|\tilde{\Psi}\rangle = e^{\hat{T}}|\tilde{\Phi}_0\rangle$, where $|\tilde{\Phi}_0\rangle$ is the X2C-transformed reference wave function, and $\hat{T}$ represents the cluster operator, which, at the CCSD level of theory, takes the form

$$\hat{T} = \sum_{ia} t_i^a \hat{a}_a^\dagger \hat{a}_i + \frac{1}{4} \sum_{ijab} t_{ij}^{ab} \hat{a}_a^\dagger \hat{a}_b^\dagger \hat{a}_j \hat{a}_i. \tag{1.3}$$

Here, the symbols $\hat{a}^\dagger$ and $\hat{a}$ represent creation and annihilation operators, respectively. At the EOM-CCSD level of theory, excited states are expanded linearly in terms of excitations out of the CCSD ground-state wave function

$$\hat{R}_I|\tilde{\Psi}\rangle = \left(r_0 + \sum_{ia} r_i^a \hat{a}_a^\dagger \hat{a}_i + \frac{1}{4} \sum_{ijab} r_{ij}^{ab} \hat{a}_a^\dagger \hat{a}_b^\dagger \hat{a}_j \hat{a}_i \right) e^{\hat{T}}|\tilde{\Phi}_0\rangle \tag{1.4}$$

The expansion coefficients r_0, r_i^a, and r_{ij}^{ab}, are obtained by solving the right-hand eigenvalue problem

$$\bar{H}_{\mathrm{N}} \hat{R}_I|\tilde{\Phi}_0\rangle = \omega_I \hat{R}_I|\tilde{\Phi}_0\rangle \tag{1.5}$$

where $\bar{H}_{\mathrm{N}} = e^{-\hat{T}} \hat{H} e^{\hat{T}} - E_{\mathrm{CC}}$ is the normal-ordered similarity-transformed Hamiltonian, E_{CC} is the ground-state energy, and ω_I is the difference between the energy of I^{th} excited state and E_{CC}. The non-hermiticity of $\bar{H}_{\mathrm{N}}$ implies the existence of left-hand excited-state wave functions, the knowledge of which is necessary for the evaluation of excited-state properties (*i.e.*, oscillator strengths). The left-hand excited-state wave functions are expanded in the same manner as the right-hand wave functions, yielding:

$$\langle\tilde{\Phi}_0|\hat{L}_I e^{-\hat{T}} = \langle\tilde{\Phi}_0| \left(l_0 + \sum_{ia} l_a^i \hat{a}_i^\dagger \hat{a}_a + \frac{1}{4} \sum_{ijab} l_{ab}^{ij} \hat{a}_i^\dagger \hat{a}_j^\dagger \hat{a}_b \hat{a}_a \right) e^{-\hat{T}} \tag{1.6}$$

with $\hat{L}_I$ satisfying:

$$\langle\tilde{\Phi}_0|\hat{L}_I \bar{H}_{\mathrm{N}} = \langle\tilde{\Phi}_0|\hat{L}_I \omega_I. \tag{1.7}$$

Note that right- and left-hand ground state wave functions can be recovered from Eqs. 2.6 and 1.6 with the choices $\hat{R}_0 = 1$ and $\hat{L}_0 = 1 + \hat{\Lambda}$, where $\hat{\Lambda}$ is the usual ground-state de-excitation operator, defined at the CCSD level of theory as:

$$\hat{\Lambda} = \sum_{ia} \lambda_a^i \hat{a}_i^\dagger \hat{a}_a + \frac{1}{4} \sum_{ijab} \lambda_{ab}^{ij} \hat{a}_i^\dagger \hat{a}_j^\dagger \hat{a}_b \hat{a}_a \tag{1.8}$$

The t- and λ-amplitudes in Eqs. 2.4 and 2.5 are determined by using a conventional CCSD algorithm,[18, 111, 34] augmented to account for complex arithmetic and spin-broken amplitudes. For low-energy excited-states, the right- and left-hand excited-state wave functions are determined via a modified Davidson algorithm[21, 40, 13, 123], which can handle complex arithmetic. For the higher energy excited states relevant to core-level excitations, these wave functions are be determined using the Generalized Preconditioned Locally Harmonic Residual (GPLHR) approach.[120, 112] The full set of equations used for this EOM-CCSD implementation can be found in the appendix in Ch. A.

1.2.3 Properties: Oscillator Strength

In order to obtain the oscillator strength of each excitation for X2C-EOM-CCSD, we first need to obtain the r- and l-amplitudes (r_0, r_i^a, r_{ij}^{ab}, l_0, l_a^i, and l_{ab}^{ij} for EOM-CCSD) from the left and right eigenvectors of the Hamiltonian. These r- and l-amplitudes are then used to create transition density matrices, which are then used to calculate properties as described in Ref. 110. Since $\bar{H}$ is non-Hermitian, we must build both transition density matrices, ρ_{pq} and ρ_{pq}, in order to calculate the oscillator strength for the transition from state I to state J. The reduced n-particle transition density matrix is defined as:

$$\rho_{IJ,pq\ldots rs} = \langle \phi_0 | \hat{L}_I e^{-T} p^\dagger q^\dagger \ldots r s e^T \hat{R}_J | \phi_0 \rangle \tag{1.9}$$

where I and J are the ground and excited state described by this particular transition density matrix. More specifically, $\rho_{IJ,pq}$ is as follows:

$$\rho_{IJ,pq} = \begin{bmatrix} \rho_{ij} & \rho_{ia} \\ \rho_{ai} & \rho_{ab} \end{bmatrix} \tag{1.10}$$

where each sub-block is represented by:

$$\begin{aligned} \rho_{ij} &= r_0(t_i^e l_e^j - \frac{1}{2} t_{im}^{fe} l_{fe}^{jm}) - r_i^e l_e^j \\ &\quad - \frac{1}{2} r_{im}^{fe} l_{fe}^{jm} - t_i^f r_m^e l_{fe}^{jm} \end{aligned} \tag{1.11}$$

$$\begin{aligned} \rho_{ab} &= r_0(t_m^b l_a^m + \frac{1}{2} t_{mn}^{eb} l_{mn}^{ea}) + r_m^b l_a^m \\ &\quad + \frac{1}{2} r_{mn}^{eb} l_{ea}^{mn} + t_n^b r_m^e l_{ea}^{mn} \end{aligned} \tag{1.12}$$

$$\rho_{ia} = r_0 l_a^i + l_{ae}^{im} r_m^e \tag{1.13}$$

$$\begin{aligned} \rho_{ai} &= r_0(t_{im}^{ae} l_e^m - t_i^e t_m^a l_e^m - \frac{1}{2} t_{in}^{ef} t_m^a l_{ef}^{mn} \\ &\quad - \frac{1}{2} t_{mn}^{af} t_i^e l_{ef}^{mn}) + l_0 r_i^a + r_{im}^{ae} l_e^m \\ &\quad - t_m^a r_i^e l_e^m - t_i^e r_m^a l_e^m \\ &\quad - \frac{1}{2} t_{mn}^{af} r_i^e l_{ef}^{mn} - \frac{1}{2} t_{in}^{ef} r_m^a l_{ef}^{mn} \\ &\quad - \frac{1}{2} r_{mn}^{af} t_i^e l_{ef}^{mn} - \frac{1}{2} r_{in}^{ef} t_m^a l_{ef}^{mn} \\ &\quad - t_i^e t_m^a r_n^f l_{mn}^{ef} - t_{im}^{ae} r_n^f l_{ef}^{mn} \end{aligned} \tag{1.14}$$

The dipole strength is then defined as:

$$D = \langle \tilde{\Psi}_I | \mu | \Psi_J \rangle \langle \tilde{\Psi}_J | \mu | \Psi_I \rangle \tag{1.15}$$

and is more directly calculated as:

$$D = \sum_{\xi} Tr(\rho_{IJ}\mu_{\xi})Tr(\rho_{JI}\mu_{\xi}) \tag{1.16}$$

where μ_{ξ} is the matrix representation of a Cartesian component of the dipole operator ($\xi \in x, y, z$). From there, the oscillator strength is calculated as:

$$f_L = \frac{2}{3}\omega D \tag{1.17}$$

where ω is the excitation energy from state I to state J. It should be noted that there is no guarantee that the oscillator strength will be non-negative or real-valued. It has been seen that negative or complex-valued oscillator strength values emerge when the Hamiltonian produces complex energies [128]. Additionally, negative energies have been seen when using geometries that are far from equilibrium with a Kramer's restricted reference wavefunction; however, these particular cases it was fixed by using a lower energy, spin-broken reference wavefunction.

1.3 Results and Discussion

The Kramers-unrestricted relativistic X2C-EOM-CCSD procedure is implemented in the Chronus Quantum software package [126]. In the current implementation, the construction of sigma vectors is powered by the Tiled-Array [11] library. The Davidson procedure, generalized for complex arithmetic, is used for iterative diagonalization of the EOM-CC Hamiltonian, in order to get the low energy roots.

1.3.1 Atomic Absorption Spectra

In this section we analyze various atomic spectra for fine-structure splittings and associated oscillator strengths caused by the spin-orbit coupling which is included variationally in the X2C reference. For atoms with the ${}^2S_{\frac{1}{2}}$ configuration, the ground state is doubly degenerate

Table 1.1: X2C-EOM-CCSD computed energy (ω, eV) and oscillator strength values (f) for the first 7 states of the sodium atom using the Sapporo-DZ-2012-All basis set[91, 31, 105, 80].

State	ω	f
1	0.000001	0.0000
2	2.086658	0.0104
3	2.086939	0.0214
4	2.088674	0.0000
5	2.089065	0.0118
6	2.089347	0.0229
7	2.089579	0.0333

with $M_J = \pm\frac{1}{2}$. As expected, the solution of X2C-EOM-CC recovers the degenerate ground state with zero oscillator strength. The first group of excited states arises from the ${}^2S_{\frac{1}{2}} \rightarrow {}^2P_{\frac{1}{2}}$ and ${}^2S_{\frac{1}{2}} \rightarrow {}^2P_{\frac{3}{2}}$ transitions, shown in Fig. 1.1 for the sodium atom. As a result of the selection rule, $\Delta M_J = 0, \pm 1$, transitions from the $M_J = \frac{1}{2}$ ground state to the $M_J = \pm\frac{1}{2}$ microstates of the ${}^2P_{\frac{1}{2}}$ manifold are all allowed, as shown in Tab. 1.1. However, the excitation from $M_J = \frac{1}{2}$ ground state to the $M_J = -\frac{3}{2}$ microstate of the ${}^2P_{\frac{3}{2}}$ manifold is forbidden. These characteristic excitations and associated oscillator strengths are correctly predicted by X2C-EOM-CC. In addition, although the calculations are done in the Kramers-unrestricted framework, time-reversal symmetries and degeneracies of excited states are mostly recovered in the EOM-CC approach, *e.g.*, 2 for the ${}^2P_{\frac{1}{2}}$ manifold and 4 for the ${}^2P_{\frac{3}{2}}$ manifold.[47] The resulting spectrum is plotted in Fig. 1.1.

Table 1.2 and Fig. 1.2 compare the X2C-EOM-CCSD results with those obtained using linear response X2C-TDHF and X2C-TDDFT methods. Due to the limited ability to recover the broken Kramers' symmetry in the reference, both the X2C-TDDFT and X2C-TDHF results show no discernible degeneracy pattern instead of the expected 2-4 splitting that both experiment and the X2C-EOM-CCSD calculation have. As noted in the discussion of Tab. 1.1, one of the four states comprising ${}^2P_{3/2}$ does not have oscillator strength and, therefore, does not appear in Fig. 1.1

Table 1.3 and 1.4 show the absolute positions of the peak positions and splitting values

from the X2C-EOM-CCSD calculations compared to the experimental values for open shell atoms (Li, Na, K, Rb) and their isoelectronic cations (Be^+, Mg^+, Ca^+, Sr^+). Alkali metal atoms and alkaline earth metal cations all exhibit the same ${}^2S_{\frac{1}{2}} \rightarrow {}^2P_{\frac{1}{2}}$ and ${}^2S_{\frac{1}{2}} \rightarrow {}^2P_{\frac{3}{2}}$ transitions as shown in the sodium atom in Fig. 1.1. Here, we can see that the computed peak positions are in excellent agreement with experiments, showing only 0.0701 eV in mean absolute error and 0.0753 eV in standard deviation, along with a splitting mean average error of 3.6 meV, in Table 1.3.

In Table 1.4, we again see excellent agreement with experiment, where the mean average error for peak position is at 0.1405 eV and the mean average error for the peak splitting is 4.3 meV. Additionally, when comparing Table 1.3 and 1.4 we can see that the Sapporro basis set does much better than the ANO-RCC basis set, even though both are double zeta and optimized for relativistic calculations. The mean absolute error (MAE) for the Sapporro peak positions is 0.07 eV and the MAE for the peak splitting is 3.6 meV.

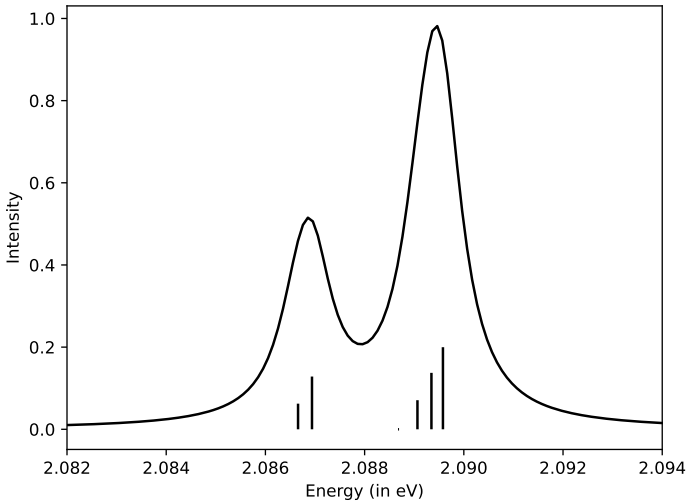

Figure 1.1: Absorption spectra of the sodium atom computed at the X2C-EOM-CCSD/Sapporro-DZ-2012-All level of theory. Numerical values are presented in Tab. 1.1. The Lorenztian broadening was used such that the full-width half-max was set to 0.014 eV.

Table 1.2: X2C-EOM-CCSD computed energy ω (eV) and oscillator strength (f) for the first 7 states of the sodium atom compared to X2C-TDHF and X2C-TDDFT, where Sapporro-DZ-2012-All[91, 31, 105] is used for the basis set and the functional used for TDDFT is X2C-BHandH.

	X2C-EOM-CCSD		X2C-TDDFT		X2C-TDHF	
State	ω	f	ω	f	ω	f
1	0.000001	0.0000	0.0000	0.0000	0.0000	0.0000
2	2.086658	0.0104	2.0689	0.0003	1.9564	0.3246
3	2.086939	0.0214	2.0696	0.0003	1.9571	0.3247
4	2.088674	0.0000	2.0703	0.0003	1.9579	0.3253
5	2.089065	0.0118	2.2055	0.3170	1.9833	0.0005
6	2.089347	0.0229	2.2061	0.3171	1.9840	0.0004
7	2.089579	0.0333	2.2068	0.3172	1.9847	0.0000

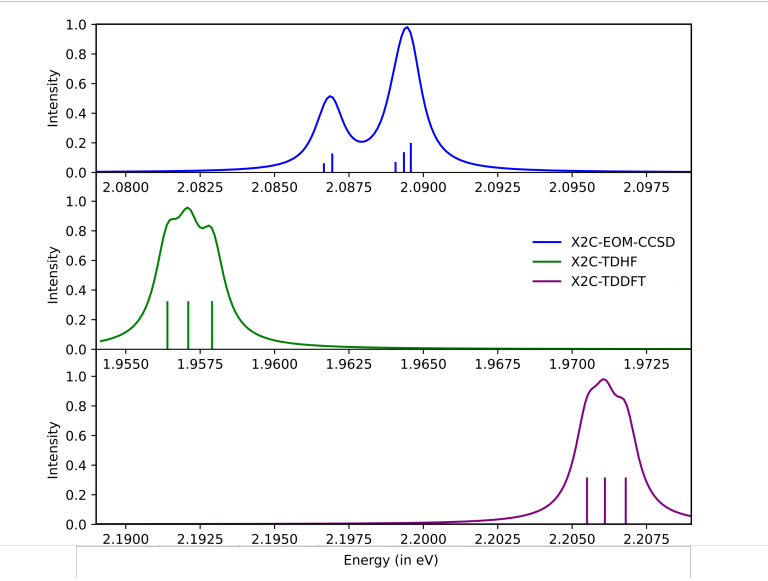

Figure 1.2: Absorption spectra of the sodium atom computed using X2C-EOM-CCSD, X2C-TDHF, and X2C-TDDFT. All spectra are computed using Sapporro-DZ-2012-All and the DFT function used is BHandH. Numerical values are presented in Tab. 1.2. The Lorenztian broadening was used such that the full-width half-max was set to 0.014 eV.

Basis set convergence was another factor considered in this benchmark. Tables 1.5 and 1.6 show calculations for the $^3D_3 \rightarrow^3 D_2$ and $^3D_2 \rightarrow^3 D_1$ transitions for copper, silver, and gold cation along with the $^3P_3 \rightarrow^3 P_2$ and $^3P_2 \rightarrow^3 P_1$ for zinc, cadmium, mercury, and their corresponding isoelectronic group 13 cations. All calculations in these tables are done with ANO-RCC using DZ, DZP, TZP, and QZP[91, 31, 105, 121, 97, 98]. Overall, improvement is observed when increasing the basis set size for both peak position and fine structure splitting, though there are several exceptions.

When looking at table 1.5, we can see that the double zeta basis set often has this best results. This phenomena where the double zeta basis will do better than a slightly larger basis is known and is often explained as getting the right answer for the wrong reasons. As more basis functions are added to the calculation, giving it more flexibility, more accurate results will be achieved. We can see that in all cases the position is predicted better by the QZ basis than then TZ basis, which is consistent with this explanation. Looking at the mean average error for this table, QZ gives the best splitting values with a MAE for splitting of

Table 1.3: X2C-EOM-CCSD computed excitation energies in eV for the $^2S_{\frac{1}{2}} \rightarrow {}^2P_{\frac{1}{2}}$ and $^2S_{\frac{1}{2}} \rightarrow {}^2P_{\frac{3}{2}}$ transitions in open-shell atoms and their isoelectronic cations, compared with experimental values.[56] These values are calculated using the Sapporo-DZP-2012-ALL[91, 31, 105, 80] basis set.

	$^2S_{\frac{1}{2}} \rightarrow {}^2P_{\frac{1}{2}}$		$^2S_{\frac{1}{2}} \rightarrow {}^2P_{\frac{3}{2}}$	
Atom	Experiment	Calculation	Experiment	Calculation
Li	1.8478	1.9181	1.8478	1.9182
Na	2.1022	2.0868	2.1044	2.0892
K	1.6099	1.6074	1.6171	1.6153
Rb	1.5595	1.5115	1.5890	1.5354
Be^+	3.9587	4.2005	3.9595	4.2014
Mg^+	4.4224	4.4709	4.4338	4.4821
Ca^+	3.1233	3.1429	3.1510	3.1702
Sr^+	2.9403	2.8384	3.0397	2.9162

Table 1.4: X2C-EOM-CCSD computed excitation energies in eV for the $^2S_{\frac{1}{2}} \rightarrow {}^2P_{\frac{1}{2}}$ and $^2S_{\frac{1}{2}} \rightarrow {}^2P_{\frac{3}{2}}$ transitions in open-shell atoms and their isoelectronic cations, compared with experimental values.[56] Mean absolute errors (MAE) in peak position are reported. These values are calculated using the ANO-RCC-VDZ basis set[91, 31, 105, 121, 98].

	$^2S_{\frac{1}{2}} \rightarrow {}^2P_{\frac{1}{2}}$		$^2S_{\frac{1}{2}} \rightarrow {}^2P_{\frac{3}{2}}$		$^2P_{\frac{1}{2}} \rightarrow {}^2P_{\frac{3}{2}}$(meV)	
Atom	Experiment	Calculation	Experiment	Calculation	Experiment	Calculation
Li	1.8478	1.8436	1.8478	1.8437	0.0	0.1
Na	2.1022	1.9893	2.1044	1.9917	2.2	2.4
K	1.6099	1.4469	1.6171	1.4536	7.2	6.7
Rb	1.5595	1.3552	1.5890	1.3779	29.5	22.7
Be^+	3.9587	4.0706	3.9595	4.0715	0.8	0.9
Mg^+	4.4224	4.3130	4.4338	4.3231	11.4	10.1
Ca^+	3.1233	2.9420	3.1510	2.9655	27.7	23.5
Sr^+	2.9403	2.7200	3.0397	2.7982	99.4	78.2
			Position		**Splitting**	
			MAE	0.1405	**MAE**	4.3

0.0222 eV. However, looking at the individual data points for splitting errors in the table, DZ does best for predicting the splitting of Cu^+, TZ does best for Ag^+, and QZ does best for Au^+, suggesting that basis set convergence has not been achieved yet.

In table 1.6, the mean average error for QZ is the lowest at 0.0931 eV for position and 0.0416 for splitting. However, QZ is not consistently the best for each individual element. For Zn the TZ basis set provides the values closest to experiment and DZ provides the best values for Tl^+ for both splitting and position, while for In^+ QZ gives the lowest error for splitting, but DZP gives the lowest error for position. Again, this suggests that basis set convergence has not yet been reached, however the differences are on the order of meV.

Table 1.5: X2C-EOM-CCSD computed excitation energies in eV for the $^3D_3 \rightarrow^3 D_2$ and $^3D_2 \rightarrow^3 D_1$ transitions in closed-shell transition metal cations, compared with experimental values.[56] Mean absolute errors (MAE) in peak position are reported. These values are calculated using the ANO-RCC DZ, DZP, TZP, and QZP basis sets[91, 31, 105, 121, 97, 98].

	$^3D_3$	$^3D_2$	$^3D_1$	$^3D_3 \rightarrow^3 D_2$	$^3D_2 \rightarrow^3 D_1$	**Position MAE**	**Splitting MAE**
Cu^+							
DZ	2.4954	2.6215	2.7739	0.1261	0.1524	0.2121	0.0109
DZP	2.3508	2.4766	2.6311	0.1258	0.1544	0.3561	0.0118
TZP	2.3278	2.4505	2.6078	0.1227	0.1572	0.3803	0.0117
QZP	2.4046	2.5288	2.6853	0.1242	0.1565	0.3027	0.0120
EXP	2.7188	2.8327	2.9754	0.1139	0.1427		
Ag^+							
DZ	4.9660	5.1838	5.5468	0.2178	0.3630	0.1217	0.0154
DZP	4.7573	4.9735	5.3484	0.2162	0.3749	0.0841	0.0119
TZP	4.5593	4.7652	5.1405	0.2059	0.3753	0.2888	0.0070
QZP	4.5697	4.7813	5.1672	0.2116	0.3858	0.2711	0.0151
EXP	4.8562	5.0518	5.4234	0.1956	0.3716		
Au^+							
DZ	1.9153	2.3085	3.5300	0.3932	1.2215	0.0865	0.0523
DZP	1.7721	2.1652	3.3970	0.3931	1.2318	0.0534	0.0470
TZP	1.6748	2.0492	3.2509	0.3744	1.2018	0.1732	0.0527
QZP	1.7379	2.1117	3.3393	0.3738	1.2276	0.1018	0.0395
EXP	1.8647	2.1872	3.4425	0.3225	1.2554		

Since these atoms and cations are all closed shell, a comparison to X2C-TDDFT is a useful benchmark. In Table 1.7, X2C-TDDFT results using the B3LYP and BP86 functionals are compared to X2C-HF, X2C-EOM-CCSD and experimental values, all using the ANO-RCC-QZP basis set[91, 31, 105]. The DFT functionals were chosen such that a GGA, a hybrid functional, and pure HF are all represented. Overall, the peak position accuracy varies greatly depending on the functional used and the atom being investigated. The largest error for EOM-CC is for the copper cation at 0.3142 eV for the $^3D_3$ peak with most errors being closer to 0.1 eV. Overall, the X2C-EOM-CCSD results have a more consistent and systematic error than X2C-TDDFT, with the absolute error getting larger for heavier atoms

Table 1.6: X2C-EOM-CCSD computed excitation energies in eV for the $^3P_3 \rightarrow ^3P_2$ and $^3P_2 \rightarrow ^3P_1$ transitions in closed-shell transition metal cations, compared with experimental values.[56] Mean absolute errors (MAE) in peak position are reported. These values are calculated using the ANO RCC DZ, DZP, TZP, and QZP basis sets[91, 31, 105, 121, 97, 98].

	$^3P_0$	$^3P_1$	$^3P_2$	$^3P_0 \rightarrow ^3P_1$	$^3P_1 \rightarrow ^3P_2$	**Position MAE**	**Splitting MAE**
Zn							
DZ	3.6408	3.6610	3.7018	0.0202	0.0407	0.3700	0.0054
DZP	3.8074	3.8286	3.8716	0.0213	0.0429	0.2020	0.0038
TZP	3.9071	3.9306	3.9785	0.0235	0.0479	0.0991	0.0002
QZP	3.9008	3.9240	3.9711	0.0232	0.0472	0.1059	0.0007
EXP	4.0061	4.0297	4.0779	0.0236	0.0482		
Cd							
DZ	3.3127	3.3685	3.4835	0.0557	0.1151	0.4386	0.0207
DZP	3.6276	3.6860	3.8079	0.0584	0.1219	0.1197	0.0160
TZP	3.6825	3.7456	3.8803	0.0630	0.1348	0.0574	0.0072
QZP	3.6849	3.7483	3.8835	0.0634	0.1352	0.0546	0.0069
EXP	3.7337	3.8009	3.9460	0.0672	0.1451		
Hg							
DZ	4.2845	4.4575	4.8304	0.1730	0.3729	0.4807	0.1237
DZP	4.7621	4.9342	5.3228	0.1721	0.3886	0.0934	0.1163
TZP	4.7961	4.9733	5.4034	0.1772	0.4301	0.0909	0.0930
QZP	4.7858	4.9721	5.4197	0.1863	0.4458	0.0822	0.0806
EXP	4.6674	4.8865	5.4606	0.2191	0.5741		
Ga^+							
DZ	5.6840	5.7397	5.8538	0.0557	0.1142	0.1892	0.0011
DZP	5.6106	5.6648	5.7760	0.0541	0.1112	0.2646	0.0030
TZP	5.7440	5.7959	5.9037	0.0519	0.1078	0.1339	0.0058
QZP	5.7852	5.8403	5.9554	0.0551	0.1151	0.0881	0.0006
EXP	5.8728	5.9282	6.0442	0.0554	0.1160		
In^+							
DZ	4.9919	5.1219	5.4012	0.1300	0.2793	0.2611	0.0156
DZP	5.2605	5.3863	5.6638	0.1257	0.2775	0.0163	0.0186
TZP	5.2577	5.3744	5.6358	0.1167	0.2614	0.0209	0.0312
QZP	5.2005	5.3270	5.6137	0.1265	0.2866	0.0524	0.0137
EXP	5.2416	5.3748	5.6821	0.1332	0.3073		
Tl^+							
DZ	6.1373	6.5038	7.4238	0.3665	0.9200	0.0811	0.1194
DZP	6.5535	6.8805	7.7780	0.3270	0.8974	0.3105	0.1488
TZP	6.4933	6.7924	7.6267	0.2991	0.8343	0.2283	0.1943
QZP	6.4111	6.7279	7.6383	0.3168	0.9104	0.1755	0.1474
EXP	6.1312	6.4960	7.6532	0.3648	1.1572		

for the peak splitting. EOMCC has a total mean average error of 0.22 eV for peak position and 0.02 eV for splitting, while B3LYP has an error of 6.01 eV for peak position and 0.24 eV for splitting. X2C-TDDFT performs especially poorly for the gold cation using both the B3LYP and BP86 functional, with the peak positions being around 17 eV away from the experimental value.

Table 1.7: X2C-TDDFT computed atomic absorption spectra (in eV) for the $^3D_3 \rightarrow^3 D_2$ and $^3D_2 \rightarrow^3 D_1$ transitions in closed-shell transition metal cations, compared with experimental values.[56] ANO-RCC-QZP is used for all calculations. Mean absolution errors (MAE) in peak position and splitting are reported.

	$^3D_3$	$^3D_2$	$^3D_1$	$^3D_3 \rightarrow^3 D_2$	$^3D_2 \rightarrow^3 D_1$	**Position MAE**	**Splitting MAE**
Cu^+							
B3LYP	1.8182	1.9543	2.1051	0.1361	0.1508	0.8831	0.0151
BP86	1.3266	1.4658	1.6108	0.1392	0.1450	1.3746	0.0138
HF	3.8674	4.0389	4.2266	0.1714	0.1877	1.5462	0.6094
EOMCC	2.4046	2.5288	2.6853	0.1242	0.1565	0.3027	0.0120
EXP	2.7188	2.8327	2.9754	0.1139	0.1427		
Ag^+							
B3LYP	4.0449	4.2725	4.6325	0.2277	0.3600	0.7938	0.0219
BP86	3.7778	4.0075	4.3598	0.2296	0.3523	1.0621	0.0267
HF	5.3657	5.6356	6.0237	0.2699	0.3881	0.5645	0.0454
EOMCC	4.5697	4.7813	5.1672	0.2116	0.3858	0.2711	0.0151
EXP	4.8562	5.0518	5.4234	0.1956	0.3716		
Au^+							
B3LYP	18.7831	18.8610	18.9617	0.0779	0.1007	16.3705	0.6996
BP86	18.2577	18.3361	18.4344	0.0784	0.0983	15.8446	0.7006
HF	2.0614	2.5833	3.8027	0.5219	1.2193	0.57799	0.7423
EOMCC	1.7379	2.1117	3.3393	0.3738	1.2276	0.1018	0.0118
EXP	1.8647	2.1872	3.4425	0.3225	1.2554		

When comparing the X2C-EOM-CCSD method to X2C-TDHF, we see that the HF calculations are systematically worse, due to their lack of correlation energy, as expected. The position error in the HF calculations are often overestimated for the d-block elements. Additionally, the splitting errors are consistently overestimated, which are often more than twice

as large as the error from the EOM-CC calculation, with the largest splitting error being 0.74 eV for the gold cation.

1.3.2 Dissociation and Spectroscopic Constants of Copper Dimer

In this section, the performance of X2C-EOM-CCSD in generating multistate potential energy curves is analyzed. The calculations for the Copper dimer in this section were done using the ANO-RCC-VDZP basis set[91, 31, 105, 121, 97, 98]. The resolution of the curve is 0.5 Å at bond lengths smaller than 2.0 Å and larger than 3.0 Å, and gets progressively smaller as the minimum is approached, going to 0.01 Å between 2.0 Å and 3.0 Å, and then 0.005 Å between 2.17 Å and 2.4 Å. The vibrational constants and the average bond distances were calculated using the 5 closest data points to the minimum.

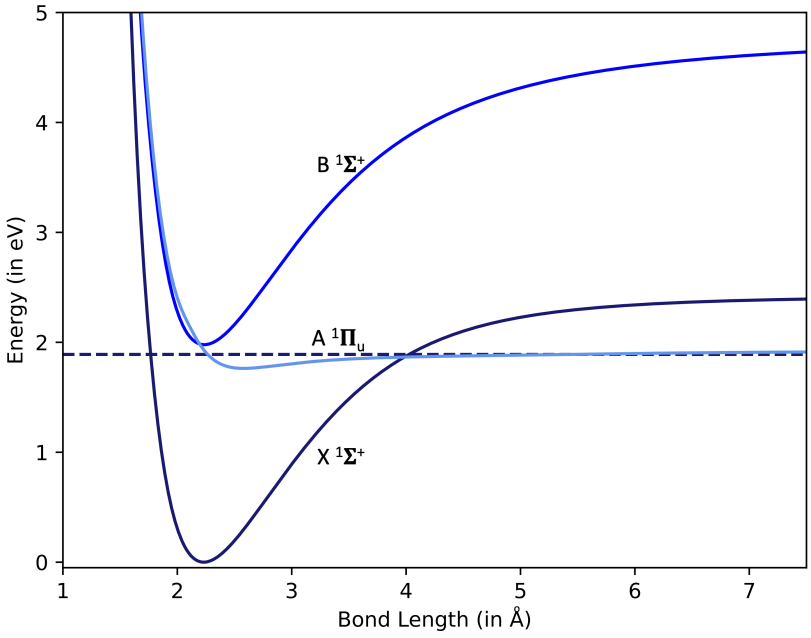

Figure 1.3: The dissociation curve for the first three states of the Copper dimer, B $^1\Sigma^+$, A $^1\Pi_u$, and X $^1\Sigma^+$.

Figure 1.3 shows the potential energy surface for the dissociation of the Copper dimer. By analyzing the data from the first few excited states of the copper dimer dissociation energy, we can see that around 4 Å, the first excited state, A $^1\Pi_u$, and the ground state swap energy ordering.

By fitting each curve with a Morse oscillator[74] of the form:

$$V(x) = D_e[1 - e^{-ax}]^2 \tag{1.18}$$

where D_e is the dissociation energy, x is the bond length and a can be used to find the force constant, k_e:

$$a = \sqrt{\frac{k_e}{2D_e}}. \tag{1.19}$$

The force constant is also equivalent to the second derivative of the Morse oscillator with respect to x. Additionally the minimum of the Morse oscillator is the equilibrium bond length, R_e, and is related to the vibrational constant, ω_e, through the following equation:

$$\omega_e = \frac{1}{2\pi}\sqrt{\frac{k_e}{m}} \tag{1.20}$$

where m is the reduced mass.

Table 1.8 shows these calculated spectroscopic constants for the first three states seen in Fig. 1.3 . For the ground state, X2C-CCSD preforms significantly better than X2C-HF, as expected. Overall, the R_e, D_e, and ω_e are in good agreement with experiment, having errors of 0.0945 eV, 0.3102 eV, and 33.91 cm^{-1} respectively. The values for T_e for the excited states are both underestimated by around 0.7 eV.

Upon closer examination of the vibrational frequencies, the error for the A $^1\Pi_u$ state is much larger than either of the $^1\Sigma^+$ states. Therefore, the vibrational frequencies were recalculated using the Colbert-Miller discrete variable representation (DVR)[17]. This resulted in similar results for the $^1\Sigma^+$ states at 257.74 cm^{-1} for X and 251.59 cm^{-1} for B. However, the A $^1\Pi_u$ state was more interesting. Though the first root from DVR was similar to the

initial calculated frequency at 96.22 cm^{-1}, the second root was suspiciously close to the experimental value at 186.2 cm^{-1}. Combined with the nonzero oscillator strength of this state near the ground state equilibrium bond length of 2.22 Å, it is possible that the experimental value for this state is for an overtone transition. This brings the mean average error for the vibrational frequency down to only 7.18 cm^{-1}.

Table 1.8: Spectroscopic constants for the dissociation of copper dimer. Experimental data taken from refs. [20, 100, 99, 4, 87, 94, 88, 22, 103, 1, 108, 46]

		T_e (eV)	R_e (Å)	D_e (eV)	ω_e (cm^{-1})
X $^1\Sigma^+$					
	X2C-CCSD	0.0000	2.23	1.9121	260.32
	X2C-HF	0.0000	2.41	-	198.25
	Expt.	0.0000	2.22	2.0832	264.55
A $^1\Pi_u$					
	X2C-EOMCCSD	1.7626	2.58	1.9121	102.98
	Expt.	2.5334	2.56	-	191.90
B $^1\Sigma^+$					
	X2C-EOMCCSD	1.9823	2.24	4.6411	251.13
	Expt.	2.6977	2.33	-	242.55
MAE					
	X2C-EOM-CCSD	0.7431	0.04	0.3102	33.91
	X2C-HF	-	0.19	0.9986	66.30

1.3.3 Phosphorescence

Phosphorescence is a radiative transition between electronic states of different spin multiplicities, most often between the first excited state triplet and the ground state singlet. While excitations between the ground state and excited states singlets are spin allowed the transitions between triplet and singlet states are spin forbidden. These excitations occur due to and spin-orbit couplings.

Phosphorescent materials, especially ones that exhibit phosphorescence at room temperature, are of great interest in a variety of fields including bioimaging and light emitting

technologies[14]. Since phosphorescence is quite sensitive to temperature, molecular aggregation, and the presence of oxygen most studies are performed in cryogenic air-proof matrices held at under 77 K[6]. This setup limits the molecular collisions due to vibrational relaxation, which is the primary cause of low quantum yields. However, the applications that are of the most interest necessitate ambient temperatures. Previously, room temperature phosphorescent materials included metal sulfides, oxides, and other inorganic compounds that are expensive and toxic, making them poorly suited for applications involving living tissue. Currently, researchers are focused on metal free organic dyes due to these materials being relatively cheap, biocompatible, easy to synthesize, and retain relatively high stability.

Therefore, the ability to accurately predict phosphorescent properties is important for the future development of new materials. Though many phosphorescent measurements have been reported and accumulated over the years, detailed descriptions of phosphorescent mechanisms are lacking, and theoretical explorations are not common[6]. Calculating phosphorescent lifetimes requires the use of excited state electronic structure calculations. Since phosphorescence is a spin forbidden triplet to singlet emission, the calculation must also include spin-orbit coupling.

In this section we calculate the phosphorescent lifetimes of various conjugated molecules as a way to benchmark X2C-EOM-CCSD. All calculations in this section were done using the ANO-RCC-VDZP [121, 97, 98, 91, 31, 105] basis set and all triplet geometries were optimized using DFT with the B3LYP functional [7, 59] and the cc-pVQZ [91, 31, 105, 25] basis set. These geometries can be found in the appendix.

The phosphorescent lifetimes of the states will be calculated using the Einstein coefficient, A_{21}, which is defined as :

$$A_{21} = \frac{1}{\tau} = \frac{64\pi^4(\Delta E)^3}{3h^4c^3}|\langle\Psi_f|\mu_{fi}|\Psi_i\rangle|^2 \tag{1.21}$$

where τ is the lifetime, ΔE is the excitation energy from the triplet to singlet state, and $\langle\Psi_f|\mu_{if}|\Psi_i\rangle|$ is the transition dipole moment between the triplet and singlet state. Since the

oscillator strength is defined as:

$$f_{fi} = \frac{2}{3}\Delta E|\langle\Psi_f|\mu_{if}|\Psi_i\rangle|^2. \tag{1.22}$$

Therefore, when all variables are in atomic units, Eq. (1.21) can be manipulated into the following form:

$$\frac{1}{\tau} = \frac{2(\Delta E)^2 f}{c^3} \tag{1.23}$$

so that the excitation energies and oscillator strength from the X2C-EOM-CCSD calculation can be used to calculate the lifetimes.

Table 1.9: Phosphorescence lifetimes of various conjugated systems. Experimental data from refs. [61, 72, 115, 114]

		ΔE (hartree)	f	τ (s)	Experimental Lifetime (s)
ethylene					11
	EOMCC	0.1643	1.04×10^{-10}	11.11	
	TDDFT	0.1489	3.00×10^{-11}	46.68	
benzene					9.83±0.15
	EOMCC	0.1193	2.09×10^{-10}	10.47	
	TDDFT	0.1111	1.08×10^{-10}	23.32	
toluene					8.3±0.15
	EOMCC	0.1156	1.49×10^{-10}	15.62	
	TDDFT	0.1067	1.93×10^{-10}	14.18	
ethylbenzene					7.79±0.13
	EOMCC	0.1150	1.44×10^{-10}	16.31	
	TDDFT	0.1059	1.38×10^{-10}	20.14	
pyradine					0.8
	EOMCC	0.0883	4.03×10^{-8}	0.10	
	TDDFT	0.0731	3.17×10^{-8}	0.18	
pyrimidine					0.01
	EOMCC	0.1226	5.01×10^{-8}	0.04	
	TDDFT	0.1126	1.32×10^{-7}	0.02	
pyrazine					0.02
	EOMCC	0.1314	1.96×10^{-7}	0.01	
	TDDFT	0.1044	3.78×10^{-8}	0.08	

Table 1.9 gives the calculated lifetimes for various phosphorescent molecules. Overall, the calculated lifetimes are a fairly good representation of the experimental lifetimes, always being on the same order of magnitude. It can be seen that the molecules with longer lifetimes, particularly those on the order of seconds, tend to have much larger errors than those with shorter lifetimes. This is likely due to the inversely proportional relationship between lifetime and oscillator strength. When the oscillator strengths are on the order of 10^{-10} or smaller, they are approaching what would be considered zero oscillator strength.

Overall EOMCC does a much better job of estimating phosphorescent lifetimes than TDDFT does, though there are exceptions. For toluene TDDFT is 1.4 s closer to the experimental value, for pyradine it is 0.085 s closer, and for pyrimidine it is 0.023 s closer. However, on average EOMCC has much smaller percent errors, with a mean percentage error of 91% verses 159% for TDDFT.

1.4 Conclusions

In this work, we introduced a framework for Kramer's unrestricted X2C-EOM-CCSD. This method was evaluated by looking at fine-structure splitting, spectroscopic constants, and phosphorescent lifetimes. Specifically, the fine structure splitting was calculated for open-shell alkali metals and their isoelectronic cations to measure the ${}^2S_{\frac{1}{2}} \rightarrow {}^2P_{\frac{1}{2}}$ and ${}^2S_{\frac{1}{2}} \rightarrow {}^2P_{\frac{3}{2}}$ splitting. Closed shell systems with ${}^3P$ and ${}^3D$ fine structure splitting were also evaluated. Overall, the calculated fine structure splitting shows good agreement with experiment and can often out-preform X2C-TDDFT. Additionally, it can maintain accuracy for open-shell systems where X2C-TDDFT often fails.

The ability to calculate spectroscopic constants was evaluated in the Copper dimer system. The equilibrium bond lengths, dissociation energies, and vibrational constants were calculated by fitting the potential energy surface curves with a Morse potential. The calculated spectroscopic constants show excellent agreement with experiment.

The application of the X2C-EOM-CCSD method to the prediction of phosphorescent lifetimes was also explored. The method has the capability to provide lifetime estimates on

the same order as the experimental values.

Chapter 2

TIME-DEPENDENT EQUATION OF MOTION COUPLED CLUSTER

This chapter has been adapted from work done by Lauren N. Koulias in collaboration with David B. Williams-Young, Daniel R. Nascimento, A. Eugene DePrince III, and Xiaosong Li. The work has been published under the title "Relativistic Real-Time Time-Dependent Equation-of-Motion Coupled-Cluster" Journal of Chemical Theory and Computation 2019 15 (12), 6617-6624. [55].

2.1 Introduction

Relativistic effects, including both scalar effects and spin-orbit coupling, have profound impacts on many photochemical processes. These effects are responsible for the manifestation of orbital contraction, increased binding energies, and inter-system crossing in molecular spectroscopies.[92, 93, 70] As such, a qualitatively correct theoretical description of the spectroscopy of heavy elements or of spin-forbidden processes requires the full consideration of both scalar relativistic and spin-orbit coupling effects. Frequency-domain quantum-chemical models built upon coupled-cluster (CC) theory[106], such as the linear response (LR)[73, 52] or equation-of-motion (EOM)[75, 29, 110] approaches, are highly accurate and widely used tools for modeling both valence- and core-electron absorption spectra.[39, 84] Relativistic frequency-domain LR- and EOM-CC calculations provide highly accurate descriptions of spin-orbit splittings, photoelectron spectra, and other excited-state properties by incorporating relativistic effects through both perturbative[15, 30, 50, 16, 12, 127, 117, 122] and variational treatments of spin-orbit couplings.[5, 107, 3, 63, 82]

While frequency-domain LR- and EOM-CC approaches have proven to be powerful tools

for the excited-state problem, the response of a molecular system to an external perturbation can also be evaluated explicitly via the integration of the time-dependent Schrödinger equation. Spectroscopic signals, such as the linear absorption spectrum, can be resolved by transforming quantum mechanical observables in the time-domain to the frequency domain. Time-domain approaches are particularly advantageous when computing a broadband spectrum of a molecular system,[78] resolving spectroscopic signatures of a region of high density of states,[118] or simulating non-equilibrium dynamics driven by a strong electromagnetic perturbation.[36] Such explicitly time-dependent approaches have become common at the Hartree-Fock and density functional theory levels (see Ref. 36 and references therein). On the other hand, the simulation of correlated electron dynamics, particularly at theCC[104, 43, 58, 101, 83] and EOM-CC[109, 69] levels of theory, are much more rare.

Given a time-dependent Hamiltonian operator, a time-dependent CC theory can be achieved by incorporating time-dependence into the CC excitation amplitudes[41, 42, 43, 83] and the underlying molecular orbital basis.[41, 42, 104, 58, 101] The molecular orbitals and CC amplitudes can then be evolved according to the time-dependent Schrödinger equation. However, because the CC wave function must satisfy a time-dependent bivariational principle,[58] the complete specification of the system at arbitrary times can only be achieved through the evolution of both the right-hand CC wave function, parameterized by the CC excitation amplitudes, and a left-hand CC wave function, which is defined in terms of both CC excitation and de-excitation amplitudes.[58, 83, 101] The CC de-excitation amplitudes also depend on time, and their time-evolution is governed by the complex conjugate of the time-dependent Schrödinger equation. Moreover, the nonlinear nature of the cluster operator leads to complicated equations for the time-evolution of the system. This latter complexity can potentially be avoided by holding the (de-)excitation amplitudes and orbitals fixed at their ground-state values and considering time-evolution of the system only at the EOM-CC level of theory.[109, 69] Indeed, Refs. 109 and 69, describe laser-driven electron dynamics modeled according to this prescription.

In this work, we employ a fundamentally different approach to time-dependent CC theory

based not on the laser-induced time-evolution of observables such as the dipole moment, but, rather, on the time-evolution of a field-free dipole autocorrelation function.[77, 78] Unlike other time-dependent CC and EOM-CC approaches, which require the time-evolution of both left- and right-hand CC wave functions, the moment-based formalism requires the explicit time-evolution of only a single quantity: either the left-hand or right-hand CC dipole moment function. Specifically, we develop a two-component relativistic extension of the time-dependent EOM-CC (TD-EOM-CC) approach outlined in Refs. 77 and 78 that is suitable for computing zero-field splitting in linear absorption spectra. Scalar and spin-orbit relativistic effects are included variationally through the exact-two-component (X2C) transformation scheme,[57, 66, 85, 44, 67, 64, 102, 62, 86, 27, 35, 54, 28, 89, 68] which requires the machinery underlying TD-EOM-CC to be generalized to handle two-component (*i.e.*, spin-broken) quantities. We then apply relativistic X2C-TD-EOM-CC with single and double excitations (EOM-CCSD) to simulate atomic absorption spectra of open-shell (Na, K, Mg^+, and Ca^+) and closed-shell (Na^+, K^+, Mg^{2+}, and Ca^{2+}) species and benchmark the accuracy of the computed splittings against those obtained from experiment.

2.2 Relativistic Two-Component Reference Wavefunction

The relativistic TD-EOM-CCSD method developed in this work utilizes spinor molecular orbitals from a relativistic two-component reference. In this Section, we present a brief review of the relativistic two-component approach; for a more thorough review on relativistic electronic structure theory, we refer readers to Refs. 26, 96, 65.

In two-component methods, the large and small components of the four-component Dirac equation are decoupled by a unitary transformation $\mathcal{U}$ that block-diagonalizes the four-component Hamiltonian:

$$\mathcal{U}^\dagger \hat{\mathcal{H}} \mathcal{U} = \begin{pmatrix} \mathbb{H}^+ & \mathbf{0}_2 \\ \mathbf{0}_2 & \mathbb{H}^- \end{pmatrix} \tag{2.1}$$

Since only the electronic solutions are of interest, only the two-component Hamiltonian corresponding to electronic solutions, $\mathbb{H}^+$, needs be computed.

Effectively, the two-component transformation eliminates the need to evaluate the small component by "folding" it into the large component:

$$\mathcal{U}\begin{pmatrix}\psi_L\\ \psi_S\end{pmatrix} = \begin{pmatrix}\tilde{\psi}_L\\ 0\end{pmatrix} \tag{2.2}$$

In this work, we use the X2C transformation approach[57, 66, 85, 44, 67, 64, 102, 62, 86, 27, 35, 54, 28, 89, 68] in which the decoupling scheme is obtained by solving the one-body four-component Dirac-Hartree-Fock equation. The two-electron term is added as the bare Coulomb operator. The leading error in this one-electron X2C approach arises from the neglect of the transformation of the two-electron Coulomb repulsion operator. To compensate for this error, an empirical correction, known as the Boettger factor, is used to scale the one-electron spin-orbit terms in order to approximately account for the two-electron spin-orbit terms[9]. This approach has been shown to be reasonably accurate in describing spin-orbit splittings of both valence and core electrons.[124, 35, 27, 28, 89, 48]

In the one-electron X2C framework, the transformation (or "picture change") is independent of the two-electron operator. This simplification gives rise to a major advantage of using an effective one-electron X2C approach in the context of post-SCF methods,[45] which is that the two-component transformation $\mathcal{U}$ becomes invariant with respect to the optimization of cluster amplitudes in the CC formalism. This nice property is due to the fact that, in the one-electron X2C framework, the four- to two-component transformation only depends on the choice of basis set through the one-electron Hamiltonian.

2.3 Equation of Motion

Throughout this Section, the labels *i,j,k,l* and *a,b,c,d* refer to molecular orbitals (MOs) that are occupied and empty in the reference configuration, respectively. Note that the nature of the relativistic Hamiltonian requires the CC equations to be formulated with complex arithmetic and generalized (spin-broken) amplitudes. Hence, unless stated otherwise, the

following discussion assumes all quantities are complex-valued and spin-broken.

The ground-state CC wave function is given by

$$|\tilde{\Psi}\rangle = e^{\hat{T}}|\tilde{\Phi}_0\rangle, \tag{2.3}$$

where $|\tilde{\Phi}_0\rangle$ is the X2C-transformed reference wave function, and $\hat{T}$ represents the cluster operator, defined at the CC with single and double excitations (CCSD) level as

$$\hat{T} = \sum_{ia} t_i^a \hat{a}_a^\dagger \hat{a}_i + \frac{1}{4}\sum_{ijab} t_{ij}^{ab} \hat{a}_a^\dagger \hat{a}_b^\dagger \hat{a}_j \hat{a}_i. \tag{2.4}$$

Here, the symbols $\hat{a}^\dagger$ and $\hat{a}$ represent creation and annihilation operators of second quantization, respectively. The CCSD de-excitation operator is similarly defined as

$$\hat{\Lambda} = \sum_{ia} \lambda_a^i \hat{a}_i^\dagger \hat{a}_a + \frac{1}{4}\sum_{ijab} \lambda_{ab}^{ij} \hat{a}_i^\dagger \hat{a}_j^\dagger \hat{a}_b \hat{a}_a. \tag{2.5}$$

The t- and λ-amplitudes in Eqs. 2.4 and 2.5 can be determined using a conventional CCSD algorithm,[18, 111, 34] modified for complex arithmetic and spin-broken amplitudes.

At the EOM-CCSD level of theory, the n^{th} electronic state is defined by single and double excitations out of the ground state:

$$\hat{R}_n|\tilde{\Psi}\rangle = (r_0 + \sum_{ia} r_i^a \hat{a}_a^\dagger \hat{a}_i + \frac{1}{4}\sum_{ijab} r_{ij}^{ab} \hat{a}_a^\dagger \hat{a}_b^\dagger \hat{a}_j \hat{a}_i) e^{\hat{T}}|\tilde{\Phi}_0\rangle. \tag{2.6}$$

Here, the expansion coefficients r_0, r_i^a, and r_{ij}^{ab}, comprise right-hand eigenfunctions of the normal-ordered similarity-transformed Hamiltonian,

$$\bar{H}_{\mathrm{N}} = e^{-\hat{T}} \hat{H} e^{\hat{T}} - E_{\mathrm{CC}} \tag{2.7}$$

that satisfy

$$\bar{H}_{\mathrm{N}} \hat{R}_n |\tilde{\Phi}_0\rangle = \omega_n \hat{R}_n |\tilde{\Phi}_0\rangle, \tag{2.8}$$

where E_{CC} represents the ground-state energy, and ω_n represents the difference between the energy of n^{th} excited state and that of the ground state. Because the similarity-transformed Hamiltonian is non-Hermitian, a set of left-hand eigenfunctions satisfying

$$\langle\tilde{\Phi}_0|\hat{L}_n\bar{H}_{\mathrm{N}} = \langle\tilde{\Phi}_0|\hat{L}_n\omega_n, \tag{2.9}$$

similarly defines the left-hand excited-state wave functions:

$$\langle\tilde{\Phi}_0|e^{-\hat{T}}\hat{L}_n = \langle\tilde{\Phi}_0|e^{-\hat{T}}(l_0 + \sum_{ia} l_a^i \hat{a}_i^\dagger \hat{a}_a + \frac{1}{4}\sum_{ijab} l_{ab}^{ij}\hat{a}_i^\dagger \hat{a}_j^\dagger \hat{a}_b \hat{a}_a). \tag{2.10}$$

The right- and left-hand wave functions for the ground state are recovered by specifying $\hat{R}_0 = 1$ and $\hat{L}_0 = 1 + \hat{\Lambda}$, respectively.

2.4 Time-Dependent Theory

Linear absorption spectra can be generated from a time-domain simulation in which one propagates the right- and left-hand CC wave functions in the presence of an oscillating electric field (for resonant or near-resonant spectra) or a delta pulse (for broadband spectra). The time-dependent dipole moment then carries information regarding the excited states that are accessed via the external perturbation. In the present formalism, however, a time-dependent external electric field is not added to the Hamiltonian directly. Rather, the absorption lineshape is extracted from the Fourier transform of the dipole autocorrelation function.

The working equations of the present approach can be obtained in the following manner,[77, 38, 71] beginning with the Fermi's Golden Rule expression for the ξ-component of the isotropic linear absorption lineshape:

$$I_\xi(\omega) = \sum_{IF} \rho_I |\langle\Psi_I|\hat{\mu}_\xi|\Psi_F\rangle|^2 \delta(E_F - E_I - \omega). \tag{2.11}$$

Here, ω is the frequency of the incident light, the sums run over all initial and final states, Ψ_I and Ψ_F, respectively, ρ_I represents the Boltzmann factor for the initial state, Ψ_I, and $\hat{\mu}_\xi$ is the component of the dipole operator that is parallel to the ξ axis ($\xi \in x, y, z$). Since, at zero Kelvin, the Boltzmann factor is zero for all excited states, we consider only the sum over final states:

$$I_\xi(\omega) = \sum_F |\langle \Psi_0 | \hat{\mu}_\xi | \Psi_F \rangle|^2 \delta(\omega_F - \omega). \tag{2.12}$$

Substituting in the ground and excited states from EOM-CC and replacing the Dirac δ with its Fourier integral, $\delta(\omega') = \int_{-\infty}^{\infty} dt\, e^{iw't}$, we obtain:

$$I_\xi(\omega) = \int_{-\infty}^{\infty} dt\, e^{-iwt} \sum_F \langle \Phi_0 | \hat{L}_0 \bar{\mu}_\xi \hat{R}_F | \Phi_0 \rangle \langle \Phi_0 | \hat{L}_F e^{i\omega_F t} \bar{\mu}_\xi \hat{R}_0 | \Phi_0 \rangle \tag{2.13}$$

where $\bar{\mu}_\xi$ represents the ξ^{th} component of the similarity-transformed dipole operator

$$\bar{\mu}_\xi = e^{-\hat{T}} \hat{\mu}_\xi e^{\hat{T}} \tag{2.14}$$

Since $\langle \Phi_0 | \hat{L}_F$ is an eigenfunction of $\bar{H}_\mathrm{N}$, we can replace $e^{i\omega_F t}$ with $e^{i\bar{H}_\mathrm{N} t}$, and then use the closure relation, $\sum_P \hat{R}_P | \Phi_0 \rangle \langle \Phi_0 | \hat{L}_p = \hat{1}$, to achieve:

$$I_\xi(\omega) = \int_{-\infty}^{\infty} dt\, e^{-iwt} \langle \Phi_0 | \hat{L}_0 \bar{\mu}_\xi e^{i\bar{H}_N t} \bar{\mu}_\xi \hat{R}_0 | \Phi_0 \rangle. \tag{2.15}$$

Right and left dipole functions can be defined such that

$$I_\xi(\omega) = \int_{-\infty}^{\infty} dt\, e^{-iwt} \langle \tilde{M}_\xi(t) | M_\xi(0) \rangle. \tag{2.16}$$

or

$$I_\xi(\omega) = \int_{-\infty}^{\infty} dt\, e^{-iwt} \langle \tilde{M}_\xi(0) | M_\xi(-t) \rangle. \tag{2.17}$$

At time $t = 0$, these functions are defined as

$$\langle \tilde{M}_\xi(0)| = \langle \Phi_0|(1 + \hat{\Lambda})\bar{\mu}_\xi \tag{2.18}$$

and

$$|M_\xi(0)\rangle = \bar{\mu}_\xi|\Phi_0\rangle. \tag{2.19}$$

It is important to note that Eqs. 2.16 and 2.17 yield equivalent lineshapes, so an absorption spectrum can be obtained by propagating either the left or the right dipole function.[77] This result contrasts with standard EOM-CC theory, in which both left and right eigenvalue problems must be solved in order to determine oscillator strengths. The full set of equations used for this implementation can be found in the Appendix in Ch. A.

2.5 Results and Discussion

The real-time propagation of the relativistic X2C-TD-EOM-CCSD is implemented in the Chronus Quantum software package [125]. In the current implementation, the evaluation of the matrix-vector products (*i.e.*, the construction of sigma vectors) is powered by the Tiled-Array [11] library. All computations employed the 6-31G basis set[32, 37, 95], unless otherwise noted. It has been shown that the time-evolution of the left- and right-dipole functions gives rise to nearly identical spectroscopic observables.[77] Therefore, we choose to obtain the time-signals by propagating the right dipole function only (Eq. (2.16)), which is done using a fourth order Runge-Kutta (RK4) numerical integrator. For these calculations a step size of either 0.01 or 0.001 a.u. time is used and propagated for around 10 femtoseconds or until the spectrum is converged. The Padé transform of the dipole autocorrelation function was used to resolve the linear absorption spectra.[78, 10, 35, 48] Prior to the transformation into the frequency domain, the signal was damped using the function $e^{-\frac{1}{2}\Gamma t}$, where t is time and Γ is the FWHM. For these calculations, a damping constant of 0.00002 a.u. was used.

2.5.1 Sodium D-lines: Relativistic vs. Non-Relativistic

The lowest excitation of a sodium atom corresponds to the $^2S \rightarrow {}^2P$ electronic transition. Due to spin-orbit coupling, the six-fold degenerate ^2P term splits into $^2P_{\frac{1}{2}}$ and $^2P_{\frac{3}{2}}$ levels, giving rise to a bright doublet known as the sodium D-lines ($^2S_{\frac{1}{2}} \rightarrow {}^2P_{\frac{1}{2}}$ and $^2S_{\frac{1}{2}} \rightarrow {}^2P_{\frac{3}{2}}$). Splitting between sodium D-lines is experimentally measured to be 2.1 meV,[56] which can only be captured with an accurate relativistic electronic structure method.

The time-evolution of the dipole autocorrelation function of a sodium atom is show in Fig. 2.1(A). This series is obtained by propagating the dipole autocorrelation function forward in time, resulting in the complex-valued oscillating dipole function. This dipole function can be transformed from the time domain into the frequency domain, resulting in the absorption spectra seen in Fig. 2.1(B).

Atomic absorption spectra computed using relativistic and non-relativistic TD-EOM-CCSD are compared in Fig. 2.1(B). In the two-component TD-EOM-CCSD formalism developed here, relativistic corrections, such as the scalar relativity and spin-orbit coupling, come from the variational reference wave function. The non-relativistic TD-EOM-CCSD uses a two-component reference wave function without any relativistic correction or transformation, also known as complex generalized Hartree-Fock (ℂ-GHF). When using ℂ-GHF as the reference wave function, the resulting spectrum has a single peak for the $^2S \rightarrow {}^2P$ transition. In contrast, when a relativistic X2C reference is used, the splitting between the $P_{\frac{1}{2}}$ and $P_{\frac{3}{2}}$ states is clearly seen with an estimated splitting of ∼2.0 meV. While the peak positions appear slightly red-shifted (by ∼0.1 eV) compared to experimental values,[56] the error in the zero-field splitting is only ∼0.1 meV.

The relativistic X2C-TD-EOM-CCSD also correctly predicts the relative oscillator strength between the $^2S_{\frac{1}{2}} \rightarrow {}^2P_{\frac{1}{2}}$ and $^2S_{\frac{1}{2}} \rightarrow {}^2P_{\frac{3}{2}}$ transitions. The $^2P_{\frac{1}{2}}$ and $^2P_{\frac{3}{2}}$ states are two- and four-fold degenerate, respectively. As a result, $^2S_{\frac{1}{2}} \rightarrow {}^2P_{\frac{3}{2}}$ peak is almost twice as intense as the $^2S_{\frac{1}{2}} \rightarrow {}^2P_{\frac{3}{2}}$ transition. In contrast, since all six $^2S \rightarrow {}^2P$ transitions are degenerate in the non-relativistic limit, the height of the peak with the ℂ-GHF reference is the sum of the

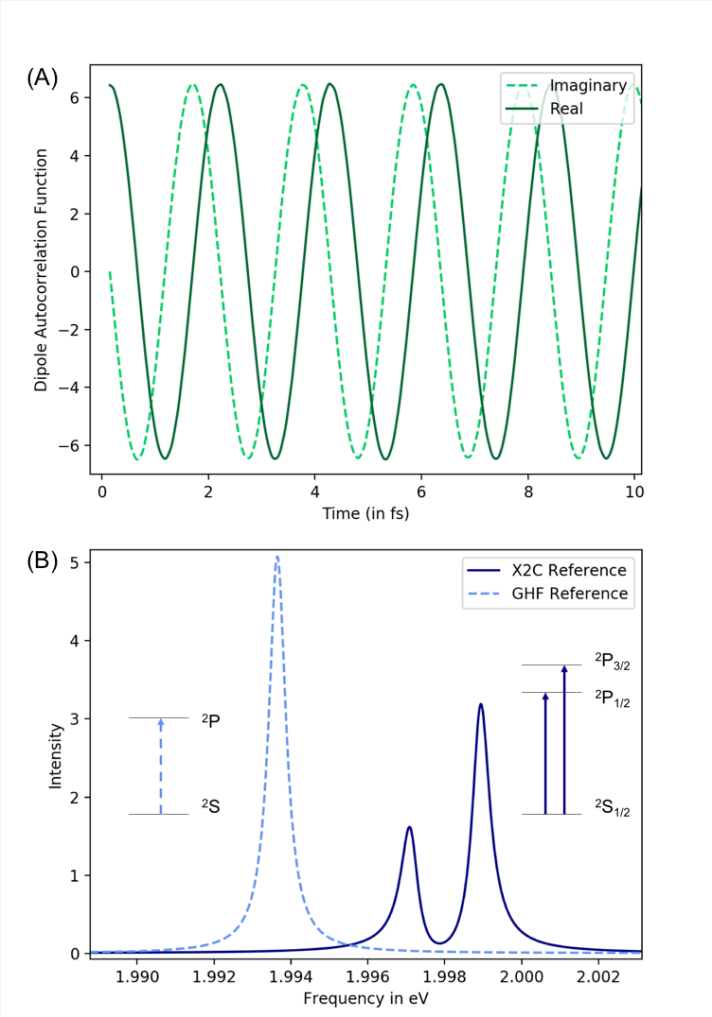

Figure 2.1: (**A**) The time propagation of both the real and imaginary parts of the dipole autocorrelation function. (**B**) Absorption spectra from TD-EOM-CCSD of a sodium atom using both the non-relativistic GHF reference and the relativistic X2C reference wave functions. Absorption spectra were obtained through Padé transformation of the dipole time signal into the frequency domain.

heights of the two peaks from the simulations with the X2C reference.

2.5.2 Zero-field Splitting of $S \rightarrow P$ Photoabsorption Spectra

To further analyze the quality of relativistic X2C-TD-EOM-CCSD, $S \rightarrow P$ excitations in a series of alkali metal atoms and alkline earth metal cations are computed. In Tab. 2.1, the excited state zero-field splitting of the calculated atomic spectra are compared to experiments. For open shell atoms (Na, K, Mg^+, Ca^+) with a single valence electron, the computed peaks correspond to $^2S_{\frac{1}{2}} \rightarrow {}^2P_{\frac{1}{2}}$ and $^2S_{\frac{1}{2}} \rightarrow {}^2P_{\frac{3}{2}}$.

Table 2.1: Zero-field splitting of atomic absorption spectra (in eV) for the $^2S_{\frac{1}{2}} \rightarrow {}^2P_{\frac{1}{2}}$ and $^2S_{\frac{1}{2}} \rightarrow {}^2P_{\frac{3}{2}}$ transitions of open-shell alkali metal atoms and alkali earth cations, computed at the X2C-TD-EOM-CCSD/6-31G level of theory and compared with experimental values.[56]

	$^2S_{\frac{1}{2}} \rightarrow {}^2P_{\frac{1}{2}}$		$^2S_{\frac{1}{2}} \rightarrow {}^2P_{\frac{3}{2}}$		$^2P_{\frac{1}{2}} \rightarrow {}^2P_{\frac{3}{2}}$(meV)	
Atom	Experiment	Calculation	Experiment	Calculation	Experiment	Calculation
Na	2.1022	1.9970	2.1044	1.9989	2.2	1.9
K	1.6099	1.4469	1.4286	1.4334	7.2	4.8
Mg^+	4.4224	4.2831	4.4338	4.2926	11.4	9.5
Ca^+	3.1233	3.1035	3.1510	3.1252	27.7	21.8
			Position		**Splitting**	
			MAE	0.0869	**MAE**	5.0

Table 2.1 shows that the computed $^2S_{\frac{1}{2}} \rightarrow {}^2P_{\frac{1}{2}}$ and $^2S_{\frac{1}{2}} \rightarrow {}^2P_{\frac{3}{2}}$ peaks are slightly red-shifted by less than 0.2 eV for neutral atoms compared to experiments. This is likely due to the small size of the basis set used in these calculations. The error in peak position decreases for atomic cations. The extra nuclear charge in cationic species gives rise to a higher degree of contraction of the electron wave function. As a result, a smaller basis set is better able to describe electronic transitions in atomic cations than in corresponding neutral atoms.

The computed zero-field splittings of the absorption peaks are in excellent agreement with experiments, with the largest error of 5.9 meV for the Ca^+ test case. As expected, the zero-

field splitting within the alkali group of atoms and the alkline earth metal cations increases with increasing principal quantum number of the valence electron. Orbital contraction in atomic cations leads to a larger spin-orbit coupling. As a result, among isoelectronic atoms (*e.g.*, Na and Mg^+), cations have a larger zero-field splitting than isoelectronic neutral atoms.

2.5.3 Photoabsorption of Spin-Forbidden Transitions

For closed shell systems, such as Na^+, K^+, Mg^{2+} and Ca^{2+}, the lowest energy excitation in non-relativistic calculations, such as those using the ℂ-GHF reference, is the spin-allowed ${}^1S \rightarrow {}^1P$ transition. In the relativistic X2C-TD-EOM-CC calculations, an additional lower energy peak appears in this spectral region (Fig. 2.2). The ${}^1S_0 \rightarrow {}^3P_1$ transition becomes dipole-allowed due to the spin-orbit coupling, but has a smaller intensity than the spin-allowed ${}^1S_0 \rightarrow {}^1P_1$ transition.

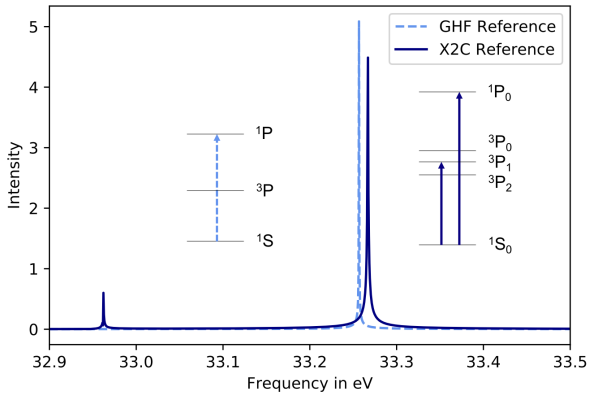

Figure 2.2: Absorption spectra from TD-EOM-CCSD/Sapporo-DZP-2012-ALL of a Na^+ using both the non-relativistic ℂ-GHF reference and the relativistic X2C reference wave functions.

Table 2.2 compares computed results using different basis sets with experiments. All computed peaks using a smaller 6-31G basis are blue-shifted by 1∼2 eV compared to the experiments. For isoelectronic closed-shell ions (*e.g.*, K^+ and Ca^{2+}), 2+ cations have a larger

Table 2.2: X2C-TD-EOM-CCSD computed atomic absorption spectra (in eV) for the $^1S_0 \rightarrow {}^3P_1$ and $^1S_0 \rightarrow {}^1P_1$ transitions in closed-shell noble gas-like cations, compared with experimental values.[56] Mean absolution errors (MAE) in peak position are reported.

	$^1S_0 \rightarrow {}^3P_1$		$^1S_0 \rightarrow {}^1P_1$		$^3P_1 \rightarrow {}^1P_1$(meV)	
Atom	Experiment	Calculation	Experiment	Calculation	Experiment	Calculation
6-31G						
Na^+	32.9413	35.1108	33.3224	35.3054	0.3811	0.1946
K^+	52.9249	54.8683	53.5029	55.2221	0.5780	0.3538
Mg^{2+}	20.2382	21.2317	20.6381	21.4773	0.3999	0.2456
Ca^{2+}	30.2435	31.0904	30.7104	31.4645	0.4669	0.3741
			Position		**Splitting**	
			MAE	1.3012	**MAE**	0.1645
Sapporo-DZP-2012-ALL						
Na^+	32.9413	32.9622	33.3224	33.2667	0.3811	0.3045
K^+	52.9249	53.0249	53.5029	53.5256	0.5780	0.5007
Mg^{2+}	20.2382	20.2357	20.6381	20.5704	0.3999	0.3347
Ca^{2+}	30.2435	30.2354	30.7104	30.6781	0.4669	0.4427
			Position		**Splitting**	
			MAE	0.2777	**MAE**	0.0608

zero-field splitting, in agreement with experiments. This is due to an increased spin-orbit coupling arising from contraction of orbitals. Calculations using the 6-31G basis set significantly overestimate the absorption peak positions by 1∼2 eV, with a larger error for smaller cations. In contrast to systems in the previous section, electronic transitions in these closed-shell atoms involve core electron excitations. The poor description of core electron wave functions using the 6-31G basis set leads to an over-contracted core electron wave function and significantly blue-shifted spectra. Increasing the size of the basis set and flexibility of core orbitals with the relativistic Sapporo-DZP-2012-ALL basis [81], the accuracy of computed spectra is drastically improved, with < 0.04 eV in mean absolute error in peak position

and < 0.08 eV in peak splitting.

For comparison, relativistic time-dependent density functional theory (X2C-TDDFT) calculations[28, 112] (Tab. 2.3) were run using the Sapporo-DZP-2012-ALL basis with the B3LYP, BP86, and BHandH functionals. Looking at the absolute peak positions, the X2C-TDDFT results are always red-shifted, with errors between $\sim$0.5 and 4.5 eV. For all results analyzed here, X2C-TD-EOM-CCSD outperforms X2C-TDDFT.

2.6 Conclusion

Here, we have discussed an implementation of relativistic X2C-TD-EOM-CCSD. By using X2C as our reference wave function, and expanding the machinery of TD-EOM-CCSD to handle two-component calculations, we are able to observe relativistic effects in the calculated absorption spectra. The approach was validated by considering the zero-field splitting in Na, Mg^+, K, and Ca^+ and the appearance of spin-forbidden transitions in Ne, Na^+, Mg^{2+}, K^+, and Ca^{2+}. By comparing these calculations to similar TD-EOM-CCSD calculations with a nonrelativistic reference, we can clearly see the splitting of peaks occurring in the open-shell species and the appearance of previously dark transitions in the open-shell species. Compared to spectra obtained by X2C-TDDFT, X2C-TD-EOM-CCSD results are consistently in better agreement with experiments.

The main advantage this method would have over a similar implementation of EOM-CCSD is that it drastically cuts down the amount of storage needed to run a calculation. While other time-dependent formalisms of EOM-CCSD would require propagation of both the left and right wave functions, this formalism only requires the propagation of either the left or right dipole function, effectively cutting the amount of computational power that would be needed in half. This implementation of X2C-TD-EOM-CCSD sets the groundwork for including electromagnetic fields, so that non-equilibrium dynamics can be simulated in the future.

Table 2.3: X2C-TDDFT computed atomic absorption spectra (in eV) for the $^1S_0 \rightarrow {}^3P_1$ and $^1S_0 \rightarrow {}^1P_1$ transitions in closed-shell noble gas-like cations, compared with experimental values.[56] Sapporo-DZP-2012-ALL is used for all calculations. Mean absolution errors (MAE) in peak position are reported.

	$^1S_0 \rightarrow {}^3P_1$		$^1S_0 \rightarrow {}^1P_1$		$^3P_1 \rightarrow {}^1P_1$(meV)	
Atom	Experiment	Calculation	Experiment	Calculation	Experiment	Calculation
TD-X2C-B3LYP						
Na^+	32.9413	30.1930	33.3224	30.5015	0.3811	0.3086
K^+	52.9249	49.4285	53.5029	49.9755	0.5780	0.5470
Mg^{2+}	20.2382	19.6621	20.6381	19.8995	0.3999	0.2375
Ca^{2+}	30.2435	28.7842	30.7104	29.2494	0.4669	0.4109
			Position		**Splitting**	
			MAE	2.1037	**MAE**	0.0855
TD-X2C-BP86						
Na^+	32.9413	29.2987	33.3224	29.5308	0.3811	0.2321
K^+	52.9249	48.8303	53.5029	49.2456	0.5780	0.4153
Mg^{2+}	20.2382	18.8295	20.6381	19.1039	0.3999	0.2744
Ca^{2+}	30.2435	28.7896	30.7104	29.2005	0.4669	0.4109
			Position		**Splitting**	
			MAE	2.7116	**MAE**	0.1233
TD-X2C-BHandH						
Na^+	32.9413	31.9982	33.3224	32.3611	0.3811	0.3629
K^+	52.9249	51.3506	53.5029	51.9756	0.5780	0.6250
Mg^{2+}	20.2382	19.8055	20.6381	20.1467	0.3999	0.3412
Ca^{2+}	30.2435	29.5461	30.7104	30.0574	0.4669	0.5113
			Position		**Splitting**	
			MAE	0.9101	**MAE**	0.1684

Chapter 3

PROPERTIES ANALYSIS OF X-RAY SPECTROSCOPY

The work in this chapter was done in collaboration with Kevin Hoang, an undergraduate computer science student at the University of Washington.

3.1 Introduction

The analysis and interpretation of experimental and theoretical spectra is an arduous task. Assigning peaks requires an in depth understanding of the system or searching through many excitations and their transition density matrices to find the major contributions to each peak in the spectra. The aim of this chapter is to explain the process of this analysis and examine the usefulness of spectral analysis tools, particularly in the realm of educational purposes.

The first section of this chapter will discuss the methods used to analyse spectra and the analysis tools that have been implemented in the FASMA library. The later half of the chapter will focus on the interpretation of x-ray spectra and how the FASMA toolbox allows students to visualize the different x-ray edges and discover how various molecular orbitals contribute to the spectra.

3.2 FASMA: A Spectral Analysis Library

FASMA (Fast Automated Spectra Modeling Analyzer) is a Python library that aims to aid in the analysis of electronic structure calculations, particularly those dealing with the generation of spectra. It is designed to be easily accessible, such that someone with basic knowledge of jupyter notebooks will find it useful. The hope is to enable both experimentalists with some data science skills and more skilled computational chemists alike, to quickly analyze the results of calculations instead of spending time on tedious data analy-

sis. The most up to date version of the library can be cloned from the Li Group github at **https://github.com/xsligroup/fasma.git**.

3.2.1 Output Parser

In the FASMA package, an efficient method for parsing lengthy output files from electronic structure packages has been developed. These files can often reach several gigabytes in size with the end of the file being comprised of many dense matrices that are necessary for further spectral evaluation. Currently the output parser works with two electronic structure packages: Gaussian[33] and ChronusQuantum[125].

The implementation of the output parser is based on a trie [24, 23], also called a prefix trie, which is a tree data structure used for locating specific keys within a set. When this data structure is used to help parse our output files, it stores the locations of certain keywords, allowing the data located with those keywords to be easily accessed and stored by our library.

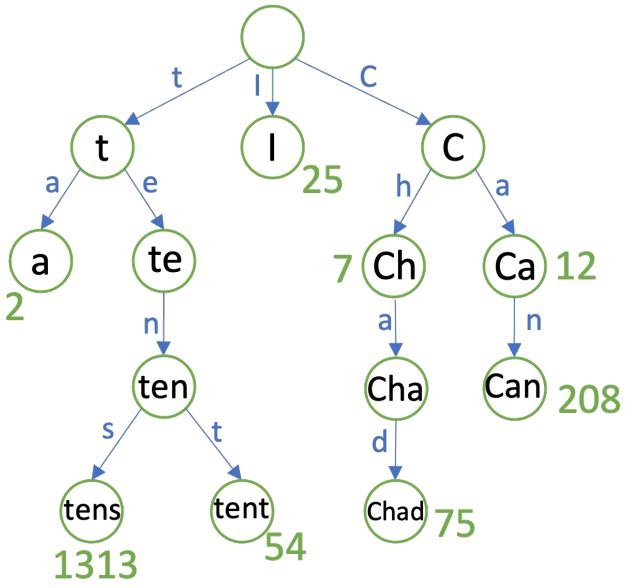

Figure 3.1: An example of the structure of a Trie data structure.

In Fig. 3.1, an example of a trie is shown. We can see that the trie starts with an empty

node and then stores strings one character at a time, allowing similar words to be compacted together. By following the path from the initial node to the bottom of the tree we can find all of the stored keywords, along with their locations. For example “ta” is located at index 2, while “Ch” is located at index 7 and “Chad” is located at index 75. The entire list of keys stored in this example trie, following a depth first search ordering, includes: “ta”, “tens”, “tent”, “I”, “Ch”, “Chad”, “Ca”, and “Can”.

Once the output file has been parsed, a Python object is created, allowing the user to easily access all of the pertinent electronic structure results in a simple Python script and quickly manipulate the results for analysis.

3.2.2 Molecular Orbital Analysis

The molecular orbital analyzer allows for a quick preliminary search of the orbitals of interest to be completed. The most common use cases include selecting an active space or as a step to determine which orbitals should be visualized. This analysis is done using the Mulliken population analysis technique [90].

First we must project the molecular orbitals back onto the basis functions:

$$b = C^* S C \tag{3.1}$$

where b is the basis function projection, C is the molecular orbital (MO) coefficient matrix, and S is the overlap matrix.

In order to determine the electron density on each atom, we can preform the following summation:

$$d_{atom} = \sum_i b_i A_i \tag{3.2}$$

where d_{atom} is the electron density for a specific type of atom, b_i is the basis function projection for orbital i, and A_i is a column vector of booleans, used to select for a specific atom

or atoms.

Similarly, to obtain the breakdown of angular momentum on each atom in the molecular orbital, we can preform the following summation:

$$d_l = \sum_i b_i L_i \tag{3.3}$$

where $d_{l,atom}$ is the electron density for a specific angular momentum value of the specified atom type and L_i is a column vector of booleans which selects a subset of the values selected by A_i. This is used to select for the specified angular momentum value.

Table 3.1: Molecular orbital analysis of an ammonia molecule based on a Hartree Fock calculation using the 6-31G basis set[32, 37, 95].

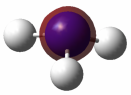	MO 1:		
	N: 0.9994	S: 0.9973	P: 0.0021
	H: 0.0006	S: 0.0006	P: 0.0000
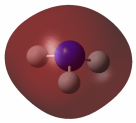	MO 3:		
	N: 0.7907	S: 0.7588	P: 0.0319
	H: 0.2093	S: 0.2093	P: 0.0000
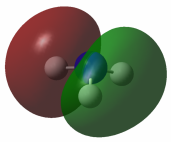	MO 5:		
	N: 0.5794	S: 0.0000	P: 0.5794
	H: 0.4205	S: 0.4205	P: 0.0000
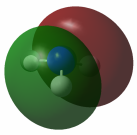	MO 7:		
	N: 0.5792	S: 0.0000	P: 0.5792
	H: 0.4208	S: 0.4208	P: 0.0000

Running this analysis using FASMA creates a Python object and generates a text file with a breakdown of each MO into the percentages of electron density on each type of atoms and then each angular momentum. For example, an MO may have 99% of the electron

density on an oxygen atom, but the electron density is split between s and p, which would suggest an sp hybridized orbital, or an MO that is below the HOMO may be 99% on a Zinc atom and have 99% d angular momentum, suggesting that it is a Zn $3d$ orbital.

Table 3.1 shows a partial example of character analysis of the ammonia molecular orbitals. Since the orbitals are paired as predicted by Kramers symmetry, only every other MO is shown in the table to avoid repetition. This table shows that MO 1 is the nitrogen $1s$ orbital, MO 3 is the $1a_1$ bonding orbital comprised of the nitrogen and hydrogen s orbitals, MO 5 and 7 are both the $1e$ bonding orbitals made up of the hydrogen s orbitals and the nitrogen p orbitals.

3.2.3 Transition Analysis

When running excited state calculations, especially in regimes where excitations beyond singles are allowed, the reduced one particle density matrix, defined as $\rho_{pq} = \langle p^\dagger q \rangle$, is a useful tool for figuring out which orbitals the electrons and holes are located in. The diagonal elements of ρ_{pq} tell us about the electron density in each MO. By taking the difference between ρ_{pq} diagonals of the initial and final states, the difference in the electron density for each MO can be seen. The ρ_{pq} difference vector will be referred to going forward as the $\delta\rho$.

The analysis of electron transitions between molecular orbitals is done by first grouping the molecular orbitals into types. Then for each type of MO the corresponding elements of $\delta\rho$ are summed together to obtain the change in electron density for that type of MO. By convention a negative value indicates where electron density is leaving from, which can be referred to as a hole, while a positive value corresponds to where the electron is going to, which can be referred to as the particle.

Projection onto the atomic orbital basis can also be a helpful tool to evaluate these electronic transitions. This process can be accomplished for each atom through the following summation:

$$t_{atom} = \sum_i \delta\rho_i d_{atom,i} \tag{3.4}$$

where t_{atom} is the electron density of the transition on a specific atom and d_{atom} is the result of Eq. 3.2. Similarly, the breakdown of the angular momentum for each transition can be obtained by:

$$t_{atom,l} = \sum_i \delta\rho_i d_{l,i} \tag{3.5}$$

where $t_{atom,l}$ is the electron density of the transition for a specific value of angular momentum on a specific type of atom.

Table 3.2: Transition Analysis of an ammonia molecule based on a CASCI calculation with an 8 electron in 10 orbital active space and the 6-31g basis set[32, 37, 95].

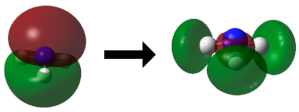

State 1 → 10	Energy: 17.976	Osc. Strength: 0.000	
	Total	Particle	Hole
$1a_1$	-0.04136	0.00000	0.04136
$1e$	-0.21579	0.00000	0.21579
$2a_1$	-0.72967	0.00000	0.72967
$3a_1$	0.76304	0.76304	0.00000
$2e$	0.22378	0.22378	0.00000

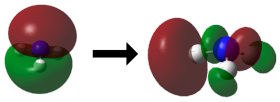

State 1 → 11	Energy: 17.976	Osc. Strength: 0.000	
	Total	Particle	Hole
$1a_1$	-0.00268	0.00000	0.00268
$1e$	-0.00479	0.00000	0.00479
$2a_1$	-0.97423	0.00000	0.97423
$3a_1$	0.00340	0.00340	0.00000
$2e$	0.97830	0.97830	0.00000

Similar to the MO analysis, the transition analysis creates a Python object and generates a text file with information about each excited state transition along with storing all of the information into a Python object. Depending on the type of analysis requested, there will

be a breakdown of each transition into either the atomic orbitals or the molecular orbitals. For example, the first excitation of water, from state 1 to state 2, may show over 99% of the electron density going from the $1b_1$ molecular orbital to the $4a_1$ molecular orbital, the expected HOMO to LUMO excitation. From this analysis, each excited state can be broken down and analyzed to discover interesting phenomena in the spectra, such as regions of spectra that are dominated by ligand to metal charge transfer or the locations of shake-up states.

Table 3.2 shows a partial example of a transition analysis for an ammonia molecule. The first transition shown is dominated by the $2a_1$ to $3a_1$ transition, while the second transition is dominated by the $2a_1$ to $2e$ transition.

3.2.4 Generating Spectra

FASMA also contains a class designed to allow both quick preliminary plotting and fully customized plotting based on the users need. There are three types of pre-made plots to choose from: absorption, character, and MO. Fig. 3.2 shows all three of the standard plotting options. The top plot is the basic absorption spectrum including both stick and broadened spectra, the middle plot is the MO breakdown, and the bottom is the character analysis or atomic orbital breakdown. The middle plot shows that the first peak is characterized as a HOMO to LUMO transition from $2a_1$ to $3a_1$ and $2e$, which matches the character analysis on the bottom of moving electron density from the nitrogen to the hydrogen. The second peak shows a transition from $1e$ and slight $2a_1$ to $2e$ and $3a1$, matching the characterization of moving from nitrogen s to nitrogen p and hydrogen s, and so on.

3.3 Silicon K-edge X-Ray Spectrum of Silicon Oxycarbides

X-ray spectroscopy is useful for a variety of reasons. By probing molecules with specific energies of x-ray light, we can gain insight into the bonding mechanisms, local molecular geometry, and local electronic structure. In practice, x-ray absorption spectroscopy (XAS) is used to study phenomena including charge transfer, oxidation states, solvation effects, and

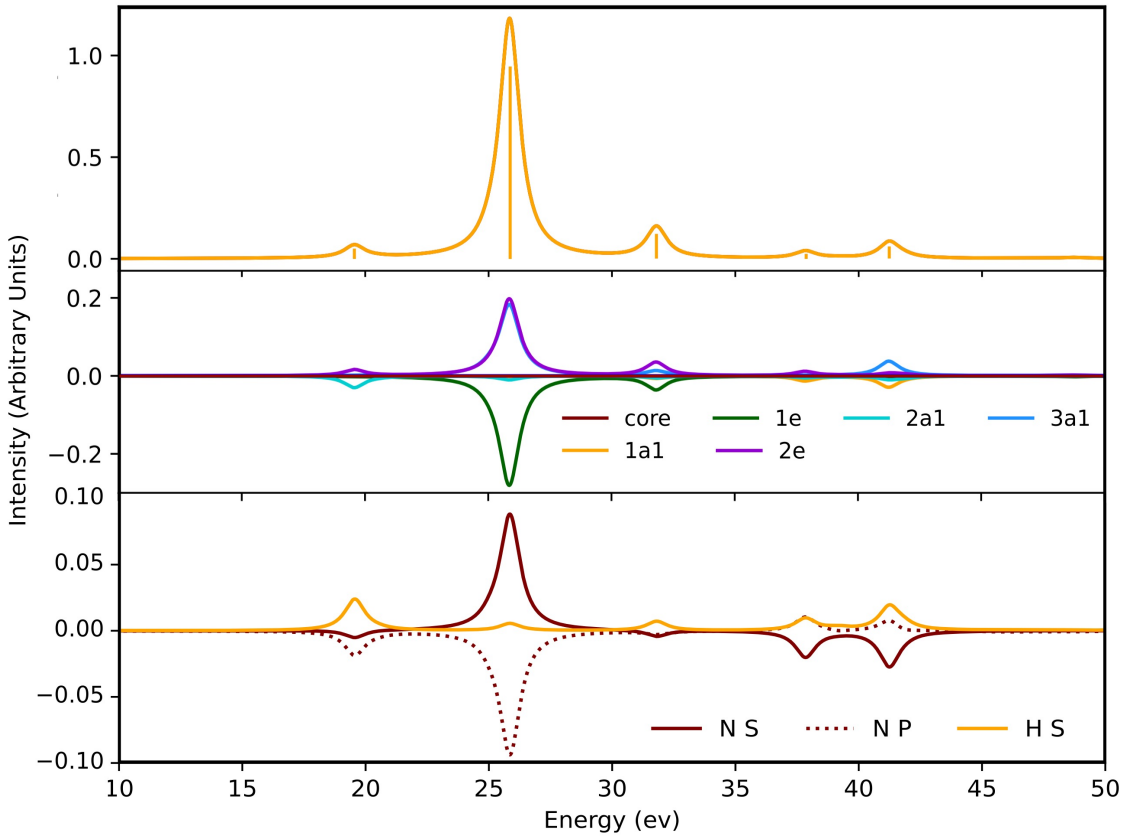

Figure 3.2: Various spectral breakdowns of ammonia.

spin crossover in metal complexes[129, 49]. Additionally, XAS is element specific, due to the large energetic separation between elements absorption regions and can be used to gather information about local molecular geometry and electronic structure.

The x-ray region of the spectra consists of excitations out of core orbitals. For the core excitations out of the $1s$ orbitals, the K-edge, relativistic effects allow the core orbitals to contract which leads to the orbital energies being lowered. This causes a uniform shift in the K-edge region of the spectra, meaning that if relativistic effects are neglected then the spectra is red-shifted, but the overall characteristics remain the same[79]. However, in the L-edge region fine-structure splitting occurs with the excitations out of the $2p_{1/2}$ and $2p_{3/2}$ orbitals, which make up the $L_{2,3}$-edge; therefore, this region is impossible to accurately

describe without including relativistic effects into the calculations, specifically spin-orbit coupling which enables the splitting of the $j = 1/2$ and $j = 3/2$ states.

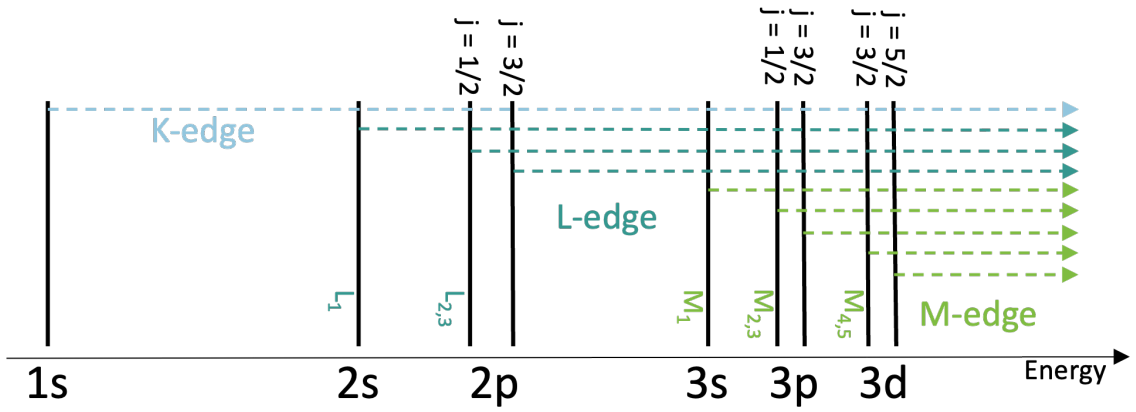

Figure 3.3: The core excitations that correspond to the various x-ray edges.

By making use of electronic structure theory, we can make in depth analyses of experimental spectra or predict what the spectra will be to determine if it will be interesting, before wasting valuable time at a synchrotron facility. The most commonly used method for generating excited state spectra is time-dependent density functional theory (TDDFT), which is the excited state extension of density functional theory[79]. This method is valued for its balance of speed and accuracy, making it suitable for most problems.

3.3.1 Silicon Oxycarbides Background Information

Silicon dioxide is an extremely important material in the semiconductor industry. The L-edge and valance band structure of various silicon materials have been of continued interest since the 1970s, arising with the beginning of the widespread computer manufacturing.

Modeling silicon dioxide theoretically was done through use of a solid-state analog to simplify the system. Before the 1990s, much of the theoretical work surrounding silicon dioxide made use of the SiO_4^{4-} ion for its solid state analog[116]. However, due to the high negative charge and many dangling bonds, this ion does not make a particularly good analog.

Tetramethoxysilane was found to make a much better analog due to its tetrahedral oxygen structure surrounding the central silicon atom and the methyl groups on the oxygens which help to simulate the environment of the oxygen being bonded to another silicon in bulk silicon dioxide.

More recently silicon oxycarbides materials have been found to have a variety of other uses. In the 1990s, polymer derived silicon oxycarbides emerged as potential anode materials[2, 113]. The mixed bonding, along with the presence of terminal hydroxyl groups, contributes to the thermodynamic stability of silicon oxycarbide polymer-derived ceramics.

In this section, we will study several small silicon oxycarbide molecules by simulating their x-ray absorption spectra, separating the spectra into the K- and L-edge, and characterizing the peaks found in the spectra based on their major MO contributions in an effort to showcase the educational potential of the FASMA library.

All TDDFT calculations throughout the rest of this chapter were done using Gaussian (g16) with the B3LYP functional[7, 59] and the cc-pVDZ basis set[91, 31, 105, 25]. The geometries used were optimized using the same functional with the cc-pVQZ basis set.

3.3.2 Locating the K- and L-edge for Si and C

Finding the various x-ray absorption edges on a theoretical spectra can be intimidating at first. The experimental energies for the edges of the various elements are well know, but these energies can be dramatically shifted in the theoretical spectra. For example, Fig. 3.4 shows the full spectra of $Si(CH_3)_4$, from a full diagonalization calculation. The grey boxes in the figure highlight where the various x-ray edges appear.

As depicted in Fig. 3.3 the K-edge comes from the core excitation of the 1s orbital, while the L-edges come from the $2s$ and $2p$ orbitals. Therefore, it is expected that the K-edge will be highest in energy and the L-edge will be lowest in energy for the core excitations. Additionally, as the element gets heavier, the excitation energy should get larger, as there is a larger gap in energy between the atoms core orbitals and unoccupied orbitals. As such, the highest energy region should be the Si K-edge, the lowest should be the Si L-edges, and

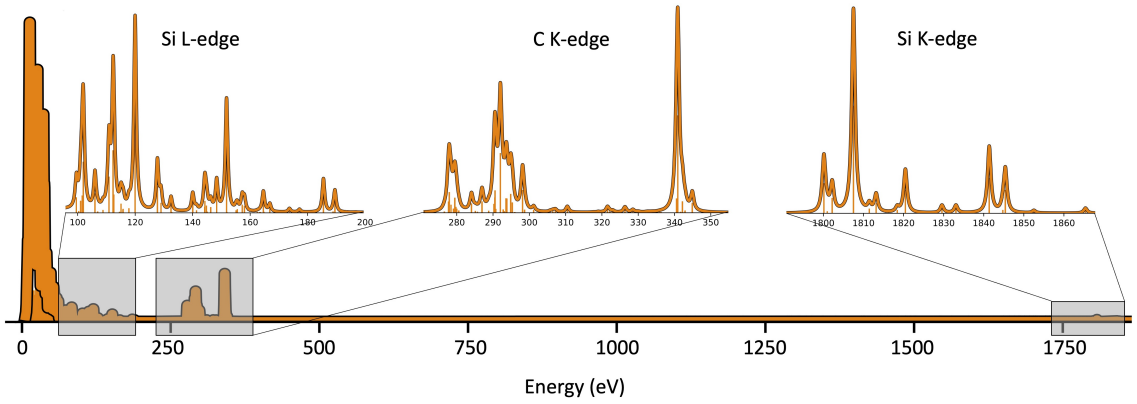

Figure 3.4: The full spectra for $Si(CH_3)_4$ with insets of the Si K- and L-edges and the C K-edge.

the middle should be the C K-edge. Experimentally, these edges are found around 1839 eV, 99 eV, and 284 eV respectively. In the theoretical spectra, the largest difference seen from experiment is the Si K-edge, which is roughly 40 eV lower in energy than expected; however, overall the energies for the three edges line up well with their experimental values.

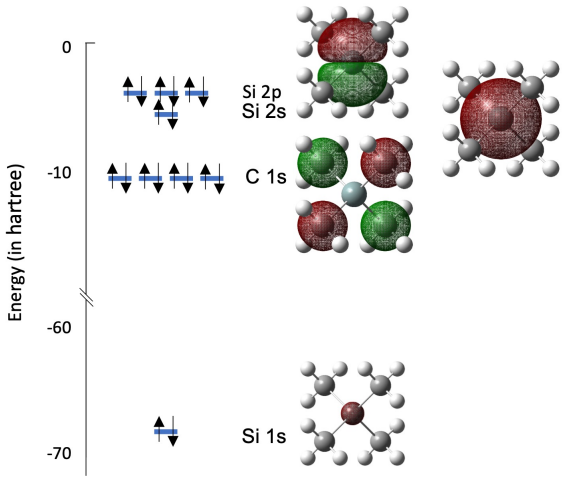

Figure 3.5: The core orbitals of the $Si(CH_3)_4$ molecule.

Additionally, this ordering can be double checked by using the FASMA library. First, the

core orbitals involved in these excitations need to be identified by MO number. Visualizing the first several MOs should give results depicted in Fig. 3.5, where MO 1 is the Si 1s orbital, MOs 2 through 5 are the C 1s orbitals, MO 6 is the Si 2s orbital, and MOs 7 through 9 are the Si 2p orbitals. This information can be put into a Python dictionary and the FASMA library can then be used to visualize the contributions from these orbitals in the spectrum.

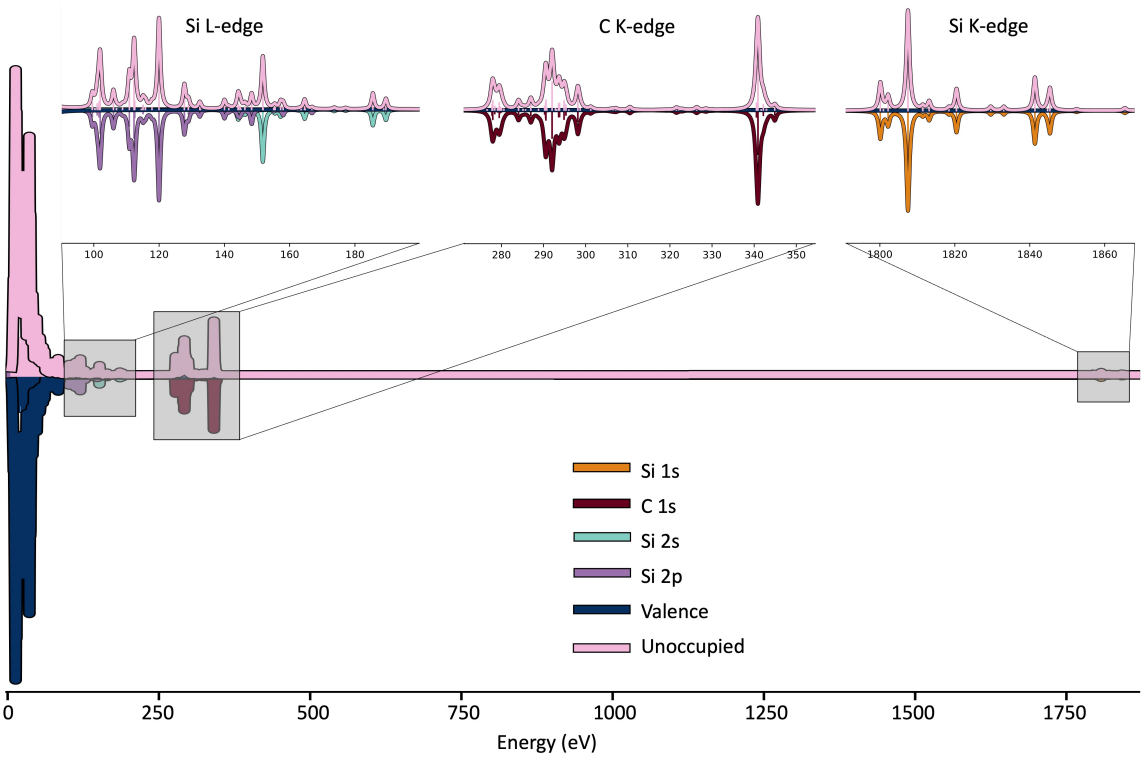

Figure 3.6: The various x-ray edges based on core orbital excitations for $Si(CH_3)_4$ with insets of the Si K- and L-edges and the C K-edge

Figure 3.6 shows the results of the MO breakdown from FASMA using these custom MO labels. The MO breakdown in this figure agrees with the assignments of the x-ray edges made previously and provides a visual way to double check. Note that in this figure the L_1-edge from the 2s orbital and $L_{2,3}$-edge from the 2p orbitals overlap each other. Typically, in heavier elements these edges would be completely separate and distinct, but silicon is a special case in this regard as one of the lightest atoms to have 2s electrons in its core, and

therefore have an L-edge x-ray spectrum. Additionally, when there is slight overlap between regions, this would allow excitations coming from different orbitals to be untangled from one another. In practice, this would be helpful for removing the extended x-ray absorption spectroscopy (EXAFS) peaks from this spectrum in the Si $L_{2,3}$-edge region, where they overlap with the pre-edge features of the next edge.

3.4 Characterizing the Peaks of the Si K-Edge

Now that it is clear where the various x-ray edges are located in the spectrum, the MOs involved in each bright transition can be found. This will be demonstrated by characterizing the peaks in the in the Si K-edge spectrum. First, the amount of information needed can be narrowed down by focusing in on the energy region for this edge, from around 1790 eV to 1870 eV.

Figure 3.7 shows the experimental and theoretical results for the silicon K-edge of silicon oxycarbides in the $Si(CH_3)_x(OCH_3)_{4-x}$ series, where $x = \{0, 1, 2, 3, 4\}$. Overall, the theoretical spectra show good agreement with experiment, with all shoulders in the peak properly represented.

3.4.1 Identifying the MOs in the K-Edge

The first step in identifying the MOs involved in each peak is the elimination of any MOs that make no contribution to the spectra in this energy region. Based on the list of MOs with nonzero contribution, a new custom dictionary can be constructed with groups of these MOs. Initially, it is a good idea to group MOs that have degenerate energies together. For example, MOs 48 through 53 all contribute to the spectra with MOs 48, 49, and 50 being at 0.50672 eV while MOs 51, 52, and 53 are at 0.50670 eV. Therefore, MOs 48 through 50 should be grouped together, and then MOs 51 through 53 should be grouped together.

Interestingly, what falls out of this is that only the triply degenerate MOs contribute to the spectra in this region. These transitions are bright due to selection rules, which state that $\Delta l = \pm 1$ and $\Delta j = \pm 1$. Therefore, if the initial state is $l = 0$, then the final state must

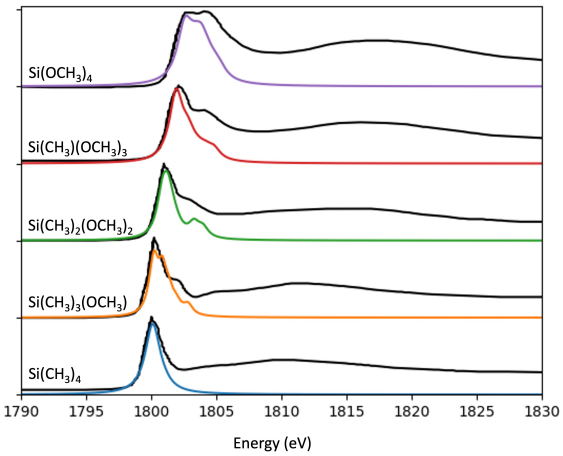

Figure 3.7: The experimental and theoretical Si K-edge of $Si(CH_3)_x(OCH_3)_{4-x}$, where $x = \{0, 1, 2, 3, 4\}$. The theoretical spectra, shown in color, were calculated using TDDFT with the B3LYP functional and the cc-pVDZ basis set. The experimental data, shown in black, is from Ref. [116]. The spectra have all been shifted by 43 eV to align with experiment.

be $l = 1$.

With the new MO dictionary created, the spectra can now be visualized with this new MO breakdown in the same manner as Fig. 3.6. In Fig. 3.8, it appears that each individual peak is governed by one main group of MOs. Some of the broadened peaks overlap, and when added all back together, the same spectra seen in Fig. 3.4 would be achieved.

3.4.2 Comparing to Experiment

When comparing theoretical and experimental x-ray absorption spectra, it is important to understand the different regions within each edge and which parts are described well by different types of theory. There are three distinct regions: the pre-edge and rising edge, which comprise x-ray absorption near edge spectroscopy (XANES), and the extended x-ray absorption fine structure (EXAFS). The XANES region can be used to determine oxidation states, molecular orbitals, band structure and coordination environment, while the EXAFS region is useful for measuring interatomic distances, near neighbour coordination numbers and lattice

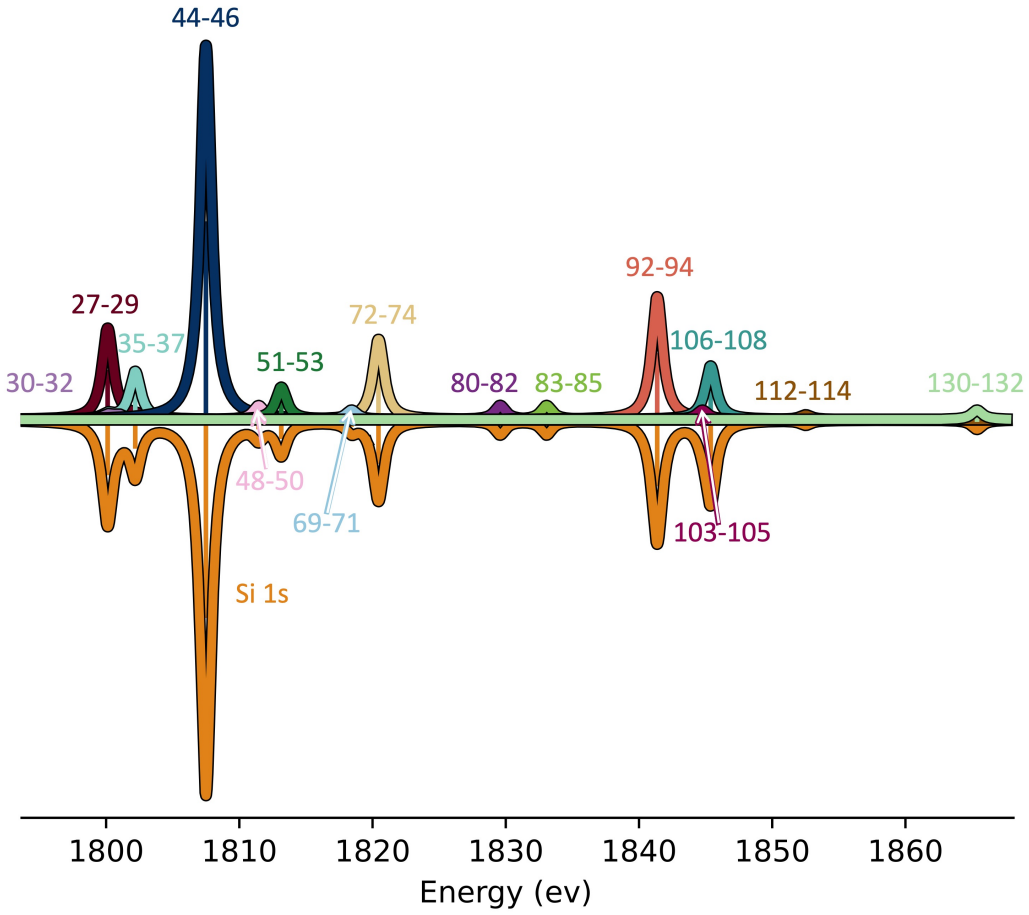

Figure 3.8: The numerical MO labels for each of the peaks in the spectral breakdown of $Si(CH_3)_4$.

dynamics. XANES is well described using electronic structure theory like what has been used in this exercise. However, EXAFS is a very different problem that cannot be solved via electronic structure theory; instead a method such as multiple scattering calculations must be preformed to describe this region [8].

This phenomena can be seen in Fig. 3.9, wherein the XANES region matches well with experiment, while the EXAFS region does not. Therefore, when conducting further analysis the EXAFS region will be excluded.

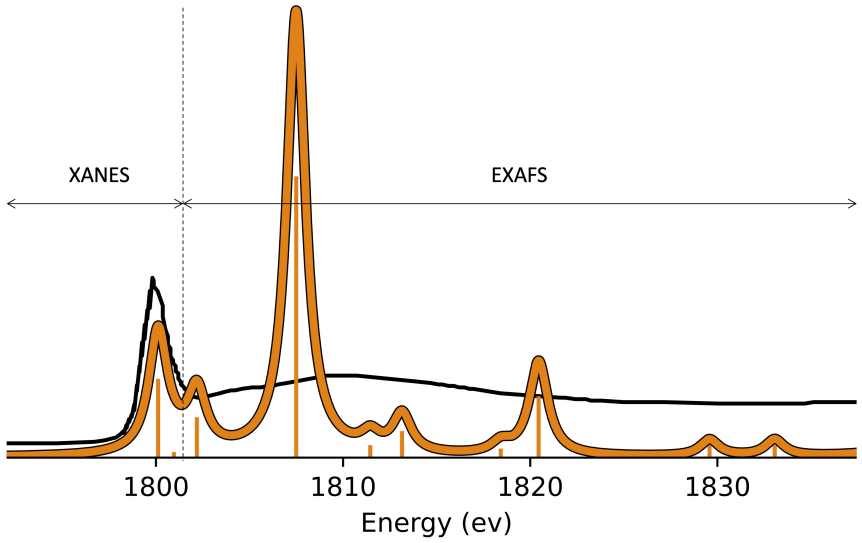

Figure 3.9: The experimental and theoretical spectra for $Si(CH_3)_4$.

3.4.3 Visualizing and Labeling the MOs using Point Group Symmetry

By visualizing and labeling the MOs below 1805 eV, the experimental peak in the Si K-edge spectrum for $Si(CH_3)_4$ can be assigned to transition from the Si 1s orbital into the 4 and $5t_2$ molecular orbitals. These orbitals and their corresponding peaks in the spectra are see in Fig. 3.10. This figure shows that the $4t_2$ orbital is responsible for the main peak, while the $5t_2$ contributes to the slight asymmetry seen in this peak. All of these orbitals move the electron density away from the silicon atom and transfer it toward the carbons in the methyl groups, with some smaller amount of electron density also being located on the hydrogens.

By repeating this process with the $x = 2$ and $x = 4$ molecules in the silicon oxycarbide series, the various peaks and shoulders in the Si K-edge can be identified. The breakdown of the $Si(CH_3)_2(OCH_3)_2$ spectra is shown in Fig. 3.11. This figure shows that the main peak is dominated by excitations to MOs 35 and 38, which are b_2 and pull the electron density away from the silicon; MOs 37 and 39 are a_1 and are higher in energy and retain electron density on the central silicon atom, while MO 36 is b_1 and is higher in energy. These higher energy excitations contribute to the increased asymmetry of the experimental peak.

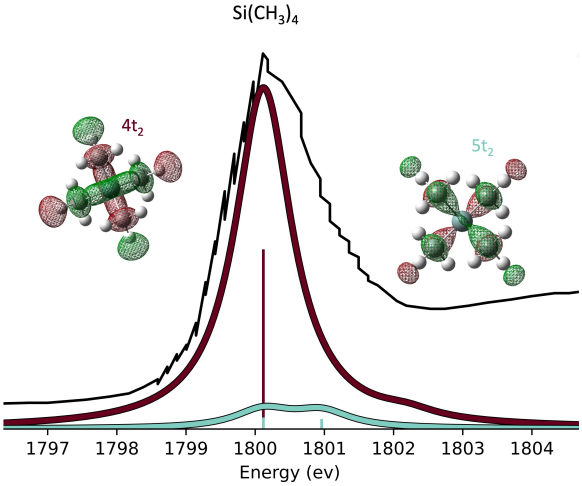

Figure 3.10: The MOs involved in the Si K-edge $Si(CH_3)_4$ XANES spectrum.

Since C_{2v} is a subgroup of T_d, and the t_2 irreducible representation of the T_d point group is comprised of the a_1, b_1, and b_2 irreducible representation of the C_{2v} point group. Going from $x = 0$ to $x = 2$ in the $Si(CH_3)_x(OCH_3)_{4-x}$ series, we can see that the different irreducible representations split from one main t_2 excitation into separate excitations to the MOs corresponding to each irreducible representation.

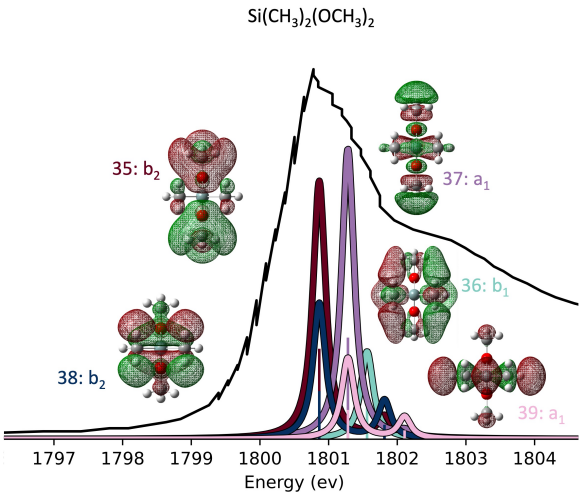

Figure 3.11: The MOs involved in the Si K-edge $Si(CH_3)_2(OCH_3)_2$ XANES spectrum.

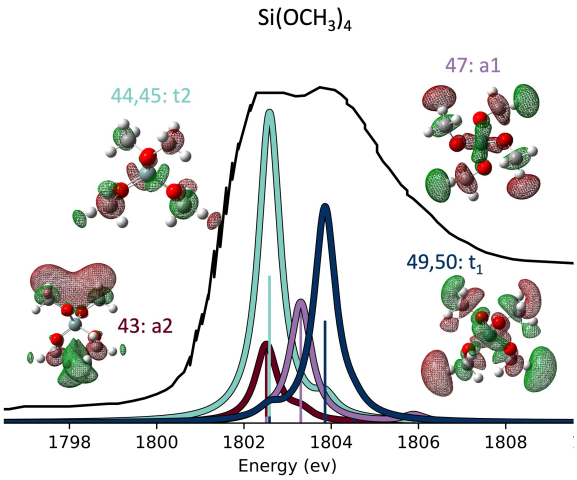

Figure 3.12: The MOs involved in the Si K-edge $Si(OCH_3)_4$ XANES spectrum.

When all four of the carbons connected to the central silicon have been replaced by oxygens, we again regain T_d symmetry in the center of the molecule, but the methyl groups on the outside of the molecule are distorted from this symmetry and more bright excitations appear in the spectra. The lowest energy peak has returned to being t_2, with contributions also coming from a_2, then there main higher energy peak that has appeared in the experimental spectrum is dominated by an excitation into the MOs corresponding to the t_1 irreducible representation.

3.5 Conclusion

In this chapter, we have presented a way to analyse spectra. We introduced FASMA library and discussed how its functionalities can be used to learn about spectra, including an in depth dive into analyzing x-ray spectra. A method to analyse molecular orbitals and electronic excitations has been discussed in detail, as well as how these breakdowns can be visualized. Identifying peaks in the silicon oxycarbide system was discussed, along with the discovery of trends as more oxygens were added to the system. Overall, this material was discussed in a manner in which an educational tutorial could be easily created.

Appendix A

A.1 CCSD Equations

The Einstein summation convention is used throughout this section.

The one-body intermediates are defined as:

$$F_{ia} = f_{ia} + t_m^e \langle im||ae\rangle \tag{A.1}$$

$$F_{ab} = f_{ab} - f_{mb} t_m^a + t_m^f \langle ma||fb\rangle - \frac{1}{2}\tau_{mn}^{ae}\langle mn||be\rangle \tag{A.2}$$

$$F_{ji} = f_{ji} + t_i^e f_{je} + t_m^e \langle jm||ie\rangle + \frac{1}{2}\tau_{im}^{ef}\langle jm||ef\rangle \tag{A.3}$$

where f_{pq} are the elements of the fock matrix, t_i^a and t_{ab}^{ij} are the T_1 and T_2 amplitudes, and τ is defines as: $\tau_{ij}^{ab} = t_{ij}^{ab} + t_i^a t_j^b - t_i^b t_j^a$.

The two-body EOM-CCSD intermediates are defined as:

$$W_{klij} = \langle kl||ij\rangle + P(ij)t_j^e\langle kl||ie\rangle + \frac{1}{2}\tau_{ij}^{ef}\langle kl||ef\rangle \quad (A.4)$$

$$W_{abcd} = \langle ab||cd\rangle - P(ab)t_m^b\langle am||cd\rangle + \frac{1}{2}\tau_{mn}^{ab}\langle mn||cd\rangle \quad (A.5)$$

$$W_{aibc} = \langle ai||bc\rangle - t_m^a\langle mi||bc\rangle \quad (A.6)$$

$$W_{ijka} = \langle jk||ia\rangle + t_i^e\langle jk||feea\rangle \quad (A.7)$$

$$W_{ajib} = \langle aj||ib\rangle - t_i^e\langle aj||eb\rangle - t_m^a\langle mj||ib\rangle - (t_{im}^{ea} + t_i^e t_m^a)\langle mj||eb\rangle \quad (A.8)$$

$$W_{ijab} = \langle ij||ab\rangle \quad (A.9)$$

$$\begin{aligned} W_{abci} &= \langle ab||ci\rangle - P(ab)t_{km}^{ae}\langle im||je\rangle + \tau_{jk}^{ef}\langle ia||ef\rangle + t_{jk}^{ae}F_{ie} \\ &\quad + t_m^a W_{imjk} - P(ij)t_j^e[\langle ia||ek\rangle - t_{mk}^{af}\langle im||ef\rangle] \end{aligned} \quad (A.10)$$

$$\begin{aligned} W_{iajk} &= \langle ia||jk\rangle + P(ij)t_{km}^{ae}\langle im||je\rangle + \frac{1}{2}\tau_{jk}^{ef}\langle ia||ef\rangle + t_{jk}^{ae}F_{ie} \\ &\quad + t_m^a W_{imjk} - P(ij)t_j^e[\langle ia||ek\rangle - t_{mk}^{af}\langle im||ef\rangle] \end{aligned} \quad (A.11)$$

where P(pq) is the antisymmetry permutation operator defined as $P(pq)f(p,q) = f(p,q) - f(q,p)$.

The CCSD ground state energy is defined as:

$$E_{CCSD} - E_0 = \sum_{ia} f_{ia}t_i^a + \frac{1}{4}\sum_{aibj}\langle ij||ab\rangle t_{ij}^{ab} + \frac{1}{2}\sum_{aibj}\langle ij||ab\rangle t_i^a t_j^b \quad (A.12)$$

A.2 EOM-CCSD Equations

Full $\bar{H}$:

$$\bar{H}_{SS} = \bar{H}^{ai}_{ck} = \mathscr{W}_{kaci} - \mathscr{F}_{ki} + \mathscr{F}_{ac} \tag{A.13}$$

$$\begin{aligned}\bar{H}_{SD} = \bar{H}^{ai}_{cdkl} &= P(cd)P(kl)\delta_{ik}\delta_{ac}\mathscr{F}_{ld} \\ &+ P(kl)\delta_{ik}\mathscr{W}_{alcd} - P(cd)\delta_{ac}\mathscr{W}_{klid}\end{aligned} \tag{A.14}$$

$$\begin{aligned}\bar{H}_{DS} = \bar{H}^{abij}_{ck} &= P(ij)\delta_{ik}\mathscr{W}_{abcj} - P(ab)\delta_{ac}\mathscr{W}_{kbij} \\ &- P(ij)\mathscr{W}_{mkic}t^{ab}_{mj} + P(ab)\mathscr{W}_{bkec}t^{ae}_{ij}\end{aligned} \tag{A.15}$$

$$\begin{aligned}\bar{H}_{DD} = \bar{H}^{abij}_{cdkl} &= P(ab)P(cd)P(kl)\delta_{ac}\delta_{ik}\delta_{jl}\mathscr{F}_{bd} \\ &- P(ij)P(cd)P(kl)\delta_{ac}\delta_{bd}\delta_{ik}\mathscr{F}_{lj} \\ &+ P(kl)\delta_{ik}\delta_{jl}\mathscr{W}_{abcd} + P(cd)\delta_{ac}\delta_{bd}\mathscr{W}_{klij} \\ &+ P(ab)P(ij)P(cd)P(kl)\delta_{ac}\delta_{ik}\mathscr{W}_{lbdj} \\ &+ P(ij)P(kl)\delta_{ik}\langle cd||lm\rangle t^{ab}_{mj} \\ &+ P(ab)P(cd)\delta_{ac}\langle de||kl\rangle t^{eb}_{ij}\end{aligned} \tag{A.16}$$

or the $\bar{H}r$ matrix-vector products

$$\begin{aligned}\bar{H}r^a_i &= \sum_b r^b_i \mathscr{F}_{ab} - \sum_j r^a_j \mathscr{F}_{ij} \\ &+ \sum_{jb} r^b_j \mathscr{W}_{jabi} + \sum_{jb} r^{ab}_{ij}\mathscr{F}_{jb} \\ &- \frac{1}{2}\sum_{jkb} r^{ab}_{jk}\mathscr{W}_{jkib} + \frac{1}{2}\sum_{jbc} r^{bc}_{ij}\mathscr{W}_{ajbc}\end{aligned} \tag{A.17}$$

$$
\begin{aligned}
\bar{H}r_{ij}^{ab} &= P(ab)\sum_{k} r_k^b \mathscr{W}_{kaij} + P(ij)\sum_{c} r_i^c \mathscr{W}_{acbj} \\
&+ P(ij)\sum_{mne} r_n^e \mathscr{W}_{mnie} t_{jm}^{ab} - P(ab)\sum_{mfe} r_m^f \mathscr{W}_{amef} t_{ij}^{ab} \\
&+ P(ij)\sum_{m} r_{jm}^{ab} \mathscr{F}_{mi} + \frac{1}{2}P(ij)\sum_{mnef} r_{in}^{ef} \langle mn||ef\rangle t_{jm}^{ab} \\
&+ P(ab)\sum_{e} r_{ij}^{ae} \mathscr{F}_{be} + \frac{1}{2}P(ab) r_{mn}^{af} \langle mn||ef\rangle t_{ij}^{be} \\
&+ P(ab)P(ij)\sum_{me} r_{mj}^{ae} \mathscr{W}_{mbei} \\
&+ \frac{1}{2}\sum_{mn} r_{mn}^{ab} \mathscr{W}_{mnij} + \frac{1}{2}\sum_{ef} r_{ij}^{ef} \mathscr{W}_{abef}
\end{aligned} \tag{A.18}
$$

where r is the guess vector, P(pq) is the antisymmetry permutation operator defined as $P(pq)f(p,q) = f(p,q) - f(q,p)$, and the one-body intermediates of the Hamiltonian are defined as:

$$
\mathscr{F}_{me} = F_{me} \tag{A.19}
$$

$$
\mathscr{F}_{ae} = F_{ae} - \frac{1}{2}\sum_{m} t_m^a \mathscr{F}_{me} \tag{A.20}
$$

$$
\mathscr{F}_{mi} = F_{mi} + \frac{1}{2}\sum_{e} t_i^e \mathscr{F}_{me} \tag{A.21}
$$

where F_{pq} are the one body intermediates from CCSD.

The two-body EOM-CCSD intermediates are:

$$\mathscr{W}_{mnij} = W_{mnij} + \frac{1}{4}\sum_{ef} \tau_{ij}^{ef} \langle mn||ef\rangle \tag{A.22}$$

$$\mathscr{W}_{abef} = W_{abef} + \frac{1}{4}\sum_{mn} \tau_{mn}^{ab} \langle mn||ef\rangle \tag{A.23}$$

$$\mathscr{W}_{mbej} = W_{mbej} - \frac{1}{2}\sum_{nf} \tau_{jn}^{fb} \langle mn||ef\rangle \tag{A.24}$$

$$\mathscr{W}_{mnie} = \langle mn||ie\rangle + \sum_{f} t_i^f \langle mn||fe\rangle \tag{A.25}$$

$$\mathscr{W}_{amef} = \langle am||ef\rangle - \sum_{n} t_n^a \langle nm||ef\rangle \tag{A.26}$$

$$\begin{aligned}\mathscr{W}_{mbij} &= \langle mb||ij\rangle - \sum_{e} \mathscr{F}_{me} t_{ij}^{be} - \sum_{n} t_n^b \mathscr{W}_{mnij} + \frac{1}{2}\sum_{ef} \langle mb||ef\rangle \tau_{ij}^{ef} \\ &+ P(ij)\sum_{ne} \langle mn||ie\rangle t_{jn}^{be} + P(ij)\sum_{ejf} t_i^e \{\langle mb||ej\rangle - t_{nj}^{bf}\langle mn||ef\rangle\}\end{aligned} \tag{A.27}$$

$$\begin{aligned}\mathscr{W}_{abei} &= \langle ab||ei\rangle - \sum_{m} \mathscr{F}_{me} t_{mi}^{ab} - \sum_{f} t_i^f \mathscr{W}_{abef} + \frac{1}{2}\sum_{mn} \langle mn||ei\rangle \tau_{mn}^{ab} \\ &- P(ab)\sum_{mf} \langle mb||ef\rangle t_{mi}^{af} - P(ab)\sum_{mnf} t_m^a \{\langle mb||ei\rangle - t_{ni}^{bf}\langle mn||ef\rangle\}\end{aligned} \tag{A.28}$$

where W_{pqrs} are the two-body intermediates from CCSD and τ is defines as: $\tau_{ij}^{ab} = t_{ij}^{ab} + t_i^a t_j^b - t_i^b t_j^a$.

A.3 Triplet Geometries for Phosphorescent Molecules

Table A.1: The excited state triplet geometry for ethylene optimized using TDDFT with the B3LYP functional and the cc-pVQZ basis set

Atom	x	y	z
C	0.0000	0.0000	0.6695
C	0.0000	0.0000	-0.6695
H	0.0000	0.9289	1.2321
H	0.0000	-0.9289	1.2321
H	0.0000	0.9289	-1.2321
H	0.0000	-0.9289	-1.2321

Table A.2: The excited state triplet geometry for benzene optimized using TDDFT with the B3LYP functional and the cc-pVQZ basis set

Atom	x	y	z
C	0.757561	-1.204870	-0.000031
C	1.436935	-0.000801	0.000007
C	0.759124	1.203927	0.000026
C	-0.757574	1.204874	-0.000031
C	-1.436935	0.000795	0.000002
C	-0.759111	-1.203923	0.000030
H	1.283433	-2.146921	-0.000120
H	2.519428	-0.001494	0.000003
H	1.286113	2.145357	0.000091
H	-1.283435	2.146930	-0.000100
H	-2.519428	0.001472	-0.000001
H	-1.286111	-2.145348	0.000098

Table A.3: The excited state triplet geometry for toluene optimized using TDDFT with the B3LYP functional and the cc-pVQZ basis set

Atom	x	y	z
C	1.919456	-0.010222	-0.000018
C	1.243809	-1.211603	-0.000050
C	-0.141867	-1.251666	-0.000052
C	-0.937829	0.045408	0.000019
C	-0.238027	1.242977	0.000015
C	1.141784	1.283284	-0.000021
H	2.998301	0.023721	0.000017
H	1.803527	-2.138173	-0.000070
H	-0.678940	-2.188420	-0.000111
H	-0.795762	2.172054	0.000041
H	1.676590	2.219959	-0.000055
C	-2.414548	-0.058746	0.000086
H	-2.771873	-0.621595	-0.873080
H	-2.771790	-0.621639	0.873256
H	-2.896711	0.917492	0.000132

Table A.4: The excited state triplet geometry for ethylbenzene optimized using TDDFT with the B3LYP functional and the cc-pVQZ basis set

Atom	x	y	z
C	0.814622	-1.209483	0.000046
C	1.435347	0.018228	0.000094
C	0.693735	1.192239	0.000039
C	-0.828075	1.134513	-0.000127
C	-1.431225	-0.111968	-0.000134
C	-0.691403	-1.281068	-0.000035
H	1.385953	-2.125309	0.000060
H	2.516576	0.071103	0.000177
H	1.171903	2.160561	0.000115
H	-2.511069	-0.178972	-0.000221
H	-1.172646	-2.246520	-0.000011
C	-1.527793	2.445116	-0.000247
H	-1.167209	3.024824	0.863916
H	-1.167104	3.024718	-0.864434
C	-3.052343	2.420250	-0.000332
H	-3.443755	1.911802	0.880945
H	-3.449205	3.434768	-0.000429
H	-3.443649	1.911668	-0.881578

Table A.5: The excited state triplet geometry for pyradine optimized using TDDFT with the B3LYP functional and the cc-pVQZ basis set

Atom	x	y	z
C	1.224176	0.638022	0.038137
C	0.000681	1.350888	-0.126779
C	-1.223539	0.639053	0.038301
C	-1.195660	-0.720287	0.115933
C	1.194978	-0.721322	0.115838
H	2.158574	1.163914	0.178892
H	0.001072	2.429392	-0.144435
H	-2.157441	1.165893	0.178797
H	-2.034260	-1.354750	0.360719
H	2.032774	-1.356483	0.361559
N	-0.000648	-1.309443	-0.289158

Table A.6: The excited state triplet geometry for pyrimidine optimized using TDDFT with the B3LYP functional and the cc-pVQZ basis set

Atom	x	y	z
C	0.664685	-1.188941	-0.000059
C	1.377613	-0.000090	0.000100
C	0.664803	1.188931	-0.000048
C	-1.398490	0.000094	0.000271
H	1.113372	-2.168227	-0.000055
H	2.459080	-0.000152	0.000130
H	1.113581	2.168169	-0.000099
H	-2.478736	0.000168	-0.000342
N	-0.718422	1.124194	-0.000086
N	-0.718572	-1.124184	-0.000088

Table A.7: The excited state triplet geometry for pyrazine optimized using TDDFT with the B3LYP functional and the cc-pVQZ basis set

Atom	x	y	z
C	-1.158587	-0.693576	0.000042
C	1.158561	-0.693613	0.000002
C	1.158572	0.693598	-0.000061
C	-1.158569	0.693589	0.000082
H	-2.099516	-1.224541	-0.000132
H	2.099529	-1.224515	0.000249
H	2.099545	1.224490	0.000135
H	-2.099495	1.224564	-0.000090
N	0.000013	1.370308	-0.000030
N	-0.000001	-1.370305	-0.000049

Bibliography

[1] Marcel Ackerman, Fred E. Stafford, and Jean Drowart. Mass Spectrometric Determination of the Dissociation Energies of the Molecules AgAu, AgCu, and AuCu. *Journal of Chemical Physics*, 33(6):1784–1789, 08 2004.

[2] Evan Adamczyk, Yulia Arinicheva, Emine Bakan, Danny Bialuschewski, Rasmus Bjažrk, Daniel Bahm, Gangho Choi, Andreas Chrysanthou, Bernard Claudet, Christian Dellen, Laurie Di Giacomo, Dina Fattakhova-Rohlfing, Olivier Faugeroux, Alain Ferriasre, Thomas Fischer, Takaya Fujisaki, Julio Garcia-Fayos, Steffen Grieshammer, Antoine Grosjean, Olivier Guillon, Peter Holtappels, Chang-Hyo Hong, Wook Jo, Woo-Seok Kang, Hwang-Pill Kim, Leonard Kwati, Yasmine Lalau, Jacques Lamon, Geon-Ju Lee, William E. Lee, Christian Lenser, Cadric Leray, Jie Li, Sandra Lobe, Mieke W.J. Luiten-Olieman, Daniel E. Mack, Sanjay Mathur, Hiroshige Matsumoto, Georg Mauer, Norbert H. Menzler, Wilhelm A. Meulenberg, Simon C. Middleburgh, Sebastian Molin, Alexander Mallmann, Danielle Ngoue, Gabriel Olalde, Nitin P. Padture, Jean-Yves Peroy, Valarie Pralong, Nini Pryds, Sabastien Quoizola, Reine Reoyo-Prats, Michael J.D. Rushton, Jaechan Ryu, Antonio Gianfranco Sabato, Richard Schmuch, Josa M. Serra, Federico Smeacetto, Audrey Soum-Glaude, Roger A. De Souza, Yasuhiro Tachibana, Laurent Thomas, Adrien Toutant, David Udomsilp, Robert Vaen, Martin Winter, Michael Wolff, and Florian Zoller. *Advanced Ceramics for Energy Conversion and Storage*. Elsevier Series on Advanced Ceramic Materials. Elsevier, 2020.

[3] Yoshinobu Akinaga and Takahito Nakajima. Two-Component Relativistic Equation-of-Motion Coupled-Cluster Methods for Excitation Energies and Ionization Potentials of

Atoms and Molecules. *Journal of Physical Chemistry A*, 121(4):827–835, 2017. PMID: 28118002.

[4] N. Aslund, R.F. Barrow, W.G. Richards, and D.N. Travis. Rotational Analysis of Bands of the B-X System of Cu2 and of the A-X System of Bi2. *Arkiv för Fysik*, 30:171, 1965.

[5] Ayush Asthana, Junzi Liu, and Lan Cheng. Exact Two-Component Equation-of-Motion Coupled-Cluster Singles and Doubles Method using Atomic Mean-Field Spin-Orbit Integrals. *Journal of Chemical Physics*, 150(7):074102, 2019.

[6] Gleb Baryshnikov, Boris Minaev, and Hans Ågren. Theory and Calculation of the Phosphorescence Phenomenon. *Chemical Reviews*, 117(9):6500–6537, 2017. PMID: 28388041.

[7] Axel D. Becke. Density-Functional Thermochemistry. III. The Role of Exact Exchange. *Journal of Chemical Physics*, 98:5648–5652, 1993.

[8] Martha A. Beckwith, William Ames, Fernando D. Vila, Vera Krewald, Dimitrios A. Pantazis, Claire Mantel, Jacques Paocaut, Marcello Gennari, Carole Duboc, Marie-Noalle Collomb, Junko Yano, John J. Rehr, Frank Neese, and Serena DeBeer. How Accurately Can Extended X-ray Absorption Spectra Be Predicted from First Principles? Implications for Modeling the Oxygen-Evolving Complex in Photosystem II. *Journal of the American Chemical Society*, 137(40):12815–12834, 2015.

[9] Jonathan C. Boettger. Approximate Two-Electron Spin-Orbit Coupling Term For Density-Functional-Theory DFT Calculations Using The Douglas-Kroll-Hess Transformation. *Physical Review B*, 62:7809–7815, 2000.

[10] Adam Bruner, Daniel LaMaster, and Kenneth Lopata. Accelerated Broadband Spectra Using Transition Dipole Decomposition and Pade Approximants. *Journal of Chemical Theory and Computation*, 12(8):3741–3750, 2016. PMID: 27359347.

[11] Justus A. Calvin and Edward F. Valeev. TiledArray: A General-Purpose Scalable Block-Sparse Tensor Framework.

[12] Zhanli Cao, Zhendong Li, Fan Wang, and Wenjian Liu. Combining the Spin-Separated Exact Two-Component Relativistic Hamiltonian with the Equation-of-Motion Coupled-Cluster Method for the Treatment of Spin–Orbit Splittings of Light and Heavy Elements. *Physical Chemistry Chemical Physics*, 19:3713–3721, 2017.

[13] Marco Caricato, Gary W. Trucks, and Michael J. Frisch. A Comparison of Three Variants of the Generalized Davidson Algorithm for the Partial Diagonalization of Large Non-Hermitian Matrices. *Journal of Chemical Theory and Computation*, 6:1966–1970, 2010.

[14] Baisong Chang, Daifeng Li, Ying Ren, Chunrong Qu, Xiaojing Shi, Ruiqi Liu, Hongguang Liu, Jie Tian, Zhenhua Hu, Taolei Sun, and Zhen Cheng. A Phosphorescent Probe for in Vivo Imaging in the Second Near-Infrared Window. *Nature Biomedical Engineering*, 6(5):629–639, 2022.

[15] Lan Cheng, Fan Wang, John F. Stanton, and Jürgen Gauss. Perturbative Treatment of Spin-Orbit-Coupling within Spin-Free Exact Two-Component Theory using Equation-of-Motion Coupled-Cluster Methods. *Journal of Chemical Physics*, 148(4):044108, 2018.

[16] Ove Christiansen, Jürgen Gauss, and Bernd Schimmelpfennig. Spin-Orbit Coupling Constants from Coupled-Cluster Response Theory. *Physical Chemistry Chemical Physics*, 2:965–971, 2000.

[17] Daniel T. Colbert and William H. Miller. A Novel Discrete Variable Representation for Quantum Mechanical Reactive Scattering via the S-Matrix Kohn Method. *Journal of Chemical Physics*, 96(3):1982–1991, 02 1992.

[18] Daniel T. Crawford and Henry F. Schaefer III. *An Introduction to Coupled Cluster Theory for Computational Chemists*, volume 14. 01 2007.

[19] Esper Dalgaard and Hendrik J Monkhorst. Some Aspects of the Time-Dependent Coupled-Cluster Approach to Dynamic Response Functions. *Physical Review A*, 28(3):1217–1222, 1983.

[20] Basil deBaskerville Darwent, DS-NES, and NSR. *Bond Dissociation Energies in Simple Molecules*. NBS Publications, 1970.

[21] Ernest R Davidson. The Iterative Calculation of a Few of the Lowest Eigenvalues and Corresponding Eigenvectors of Large Real-symmetric Matrices. *Journal of Computational Physics*, 17(1):87–94, 1975.

[22] Jean Drowart and Richard E. Honig. Mass Spectrometric Study of Copper, Silver, and Gold. *Journal of Chemical Physics*, 25(3):581–582, 10 2004.

[23] Adam Drozdek. *Data Structures and Algorithms in C++*. Cengage Learning, 2012.

[24] John A. Dundas III. Implementing Dynamic Minimal-Prefix Tries. *Software: Practice and Experience*, 21(10):1027–1040, 1991.

[25] Thom H. Dunning. Gaussian Basis Sets for Use in Correlated Molecular Calculations. I. The Atoms Boron Through Neon and Hydrogen. *Journal of Chemical Physics*, 90:1007–1023, 1989.

[26] Ken G. Dyall and Knut Fægri Jr. *Introduction to Relativistic Quantum Chemistry*. Oxford University Press, 2007.

[27] Franco Egidi, Joshua J. Goings, Michael J. Frisch, and Xiaosong Li. Direct Atomic-Orbital-Based Relativistic Two-Component Linear Response Method for Calculating Excited-State Fine Structures. *Journal of Chemical Theory and Computation*, 12(8):3711–3718, 2016.

[28] Franco Egidi, Shichao Sun, Joshua J. Goings, Giovanni Scalmani, Michael J. Frisch, and Xiaosong Li. Two-Component Non-Collinear Time-Dependent Spin Density Functional Theory for Excited State Calculations. *Journal of Chemical Theory and Computation*, 13(6):2591–2603, 2017.

[29] Kurt Emrich. An Extension of the Coupled Cluster Formalism to Excited States (I) . *Nuclear Physics A*, 351(3):379 – 396, 1981.

[30] Evgeny Epifanovsky, Kerstin Klein, Stella Stopkowicz, Jürgen Gauss, and Anna I. Krylov. Spin-Orbit Couplings within the Equation-of-Motion Coupled-Cluster Framework: Theory, Implementation, and Benchmark Calculations. *Journal of Chemical Physics*, 143(6):064102, 2015.

[31] David Feller. The Role of Databases in Support of Computational Chemistry Calculations. *Journal of Computational Chemistry*, 17:1571–1586, 1996.

[32] Michelle M. Francl, William J. Pietro, Warren J. Hehre, J. Stephen Binkley, Mark S. Gordon, Douglas J. DeFrees, and John A. Pople. Self-Consistent Molecular Orbital Methods. XXIII. A Polarization-Type Basis Set for Second-Row Elements. *Journal of Chemical Physics*, 77, 1982.

[33] M. J. Frisch, G. W. Trucks, H. B. Schlegel, G. E. Scuseria, M. A. Robb, J. R. Cheeseman, G. Scalmani, V. Barone, G. A. Petersson, H. Nakatsuji, X. Li, M. Caricato, A. V. Marenich, J. Bloino, B. G. Janesko, R. Gomperts, B. Mennucci, H. P. Hratchian, J. V. Ortiz, A. F. Izmaylov, J. L. Sonnenberg, D. Williams-Young, F. Ding, F. Lipparini, F. Egidi, J. Goings, B. Peng, A. Petrone, T. Henderson, D. Ranasinghe, V. G. Zakrzewski, J. Gao, N. Rega, G. Zheng, W. Liang, M. Hada, M. Ehara, K. Toyota, R. Fukuda, J. Hasegawa, M. Ishida, T. Nakajima, Y. Honda, O. Kitao, H. Nakai, T. Vreven, K. Throssell, J. A. Montgomery, Jr., J. E. Peralta, F. Ogliaro, M. J. Bearpark, J. J. Heyd, E. N. Brothers, K. N. Kudin, V. N. Staroverov, T. A. Keith, R. Kobayashi, J. Normand, K. Raghavachari, A. P. Rendell, J. C. Burant, S. S. Iyengar,

J. Tomasi, M. Cossi, J. M. Millam, M. Klene, C. Adamo, R. Cammi, J. W. Ochterski, R. L. Martin, K. Morokuma, O. Farkas, J. B. Foresman, and D. J. Fox. Gaussian 16 Revision A.03. Gaussian Inc. Wallingford CT 2016.

[34] Jürgen Gauss and John F. Stanton. Coupled-Cluster Calculations of Nuclear Magnetic Resonance Chemical Shifts. *Journal of Chemical Physics*, 103:3561–3577, 1995.

[35] Joshua J. Goings, Joseph M. Kasper, Franco Egidi, Shichao Sun, and Xiaosong Li. Real Time Propagation of the Exact Two Component Time-Dependent Density Functional Theory. *Journal of Chemical Physics*, 145(10):104107, 2016.

[36] Joshua J. Goings, Patrick J. Lestrange, and Xiaosong Li. Real-Time Time-Dependent Electronic Structure Theory. *WIREs Computational Molecular Science*, 8(1):e1341, 2018.

[37] Mark S. Gordon, J. Stephen Binkley, John A. Pople, William J. Pietro, and Warren J. Hehre. Self-consistent molecular-orbital methods. 22. small split-valence basis sets for second-row elements. *Journal of the American Chemical Society*, 104, 1982.

[38] Roy G Gordon. Molecular Motion in Infrared and Raman Spectra. *Journal of Chemical Physics*, 43:1307–1312, 1965.

[39] Trygve Helgaker, Sonia Coriani, Poul Jørgensen, Kasper Kristensen, Jeppe Olsen, and Kenneth Ruud. Recent Advances in Wave Function-Based Methods of Molecular-Property Calculations. *Chemical Reviews*, 112(1):543–631, 2012.

[40] Kimihiko Hirao and Hiroshi Nakatsuji. A Generalization of the Davidson's Method to Large Nonsymmetric Eigenvalue Problems. *Journal of Computational Physics*, 45:246–254, 1982.

[41] P. Hoodbhoy and J. W. Negele. Time-Dependent Coupled-Cluster Approximation to Nuclear Dynamics. I. Application to a Solvable Model. *Physical Review C*, 18:2380–2394, Nov 1978.

[42] P. Hoodbhoy and J. W. Negele. Time-Dependent Coupled-Cluster Approximation to Nuclear Dynamics. II. General Formulation. *Physical Review C*, 19:1971–1982, Apr 1979.

[43] Christian Huber and Tillmann Klamroth. Explicitly Time-Dependent Coupled Cluster Singles Doubles Calculations of Laser-Driven Many-Electron Dynamics. *Journal of Chemical Physics*, 134(5):054113, 2011.

[44] Miroslaŵ Ilias and Trond Saue. An Infinite-Order Relativistic Hamiltonian by a Simple One-Step Transformation. *Journal of Chemical Physics*, 126:064102, 2007.

[45] Andrew J. Jenkins, Hongbin Liu, Joseph M. Kasper, Michael J. Frisch, and Xiaosong Li. Variational Relativistic Complete Active Space Self-Consistent Field Method. *Journal of Chemical Theory and Computation*, 15:2974–2982, 2019.

[46] P. Joyes and Mireille Leleyter. Ab Initio Study of Cu_2 and Cu_2^+. *Journal of Physics B: Atomic and Molecular Physics*, 6(1):150, 1973.

[47] Joseph M. Kasper, Andrew J. Jenkins, Shichao Sun, and Xiaosong Li. Perspective on Kramers Symmetry Breaking and Restoration in Relativistic Electronic Structure Methods for Open-Shell Systems. *Journal of Chemical Physics*, 153(9):090903, 2020.

[48] Joseph M. Kasper, Patrick J. Lestrange, Torin F. Stetina, and Xiaosong Li. Modeling $L_{2,3}$-Edge X-ray Absorption Spectroscopy with Real-Time Exact Two-Component Relativistic Time-Dependent Density Functional Theory. *Journal of Chemical Theory and Computation*, 14(4):1998–2006, 2018.

[49] Jun Kawai. *X-Ray Spectroscopy for Chemical State Analysis*. Springer Nature, 2022.

[50] Kerstin Klein and Jürgen Gauss. Perturbative Calculation of Spin-Orbit Splittings Using the Equation-of-Motion Ionization-Potential Coupled-Cluster Ansatz. *Journal of Chemical Physics*, 129(19):194106, 2008.

[51] Henrik Koch, Hans Jørgen Aa. Jensen, Poul Jørgensen, Trygve Helgaker, et al. Excitation Energies From the Coupled Cluster Singles and Doubles Linear Response Function (CCSDLR). Applications to Be, CH^+, CO, and H_2O. *Journal of Chemical Physics*, 93(5):3345–3350, 1990.

[52] Henrik Koch and Poul Jørgensen. Coupled Cluster Response Functions. *Journal of Chemical Physics*, 93:3333–3344, 1990.

[53] Henrik Koch, Rika Kobayashi, Alfredo Sanchez de Merás, and Poul Jørgensen. Calculation of Size-Intensive Transition Moments From the Coupled Cluster Singles and Doubles Linear Response Function. *Journal of Chemical Physics*, 100(6):4393–4400, 1994.

[54] Lukas Konecny, Marius Kadek, Stanislav Komorovsky, Olga L. Malkina, Kenneth Ruud, and Michal Repisky. Acceleration of Relativistic Electron Dynamics by Means of X2C Transformation: Application to the Calculation of Nonlinear Optical Properties. *Journal of Chemical Theory and Computation*, 12(12):5823–5833, Dec 2016.

[55] Lauren N. Koulias, David B. Williams-Young, Daniel R. Nascimento, A. Eugene DePrince, and Xiaosong Li. Relativistic Time-Dependent Equation-of-Motion Coupled-Cluster. *Journal of Chemical Theory and Computation*, 15:6617–6624, 2019.

[56] Alexander Kramida, Yuri Ralchenko, Joseph Reader, and NIST ASD Team. NIST Atomic Spectra Database (version 5.6.1). https://physics.nist.gov/asd, 2018. National Institute of Standards and Technology, Gaithersburg, MD.

[57] Werner Kutzelnigg and Wenjian Liu. Quasirelativistic Theory Equivalent to Fully Relativistic Theory. *Journal of Chemical Physics*, 123:241102, 2005.

[58] Simen Kvaal. Ab Initio Quantum Dynamics using Coupled-Cluster. *Journal of Chemical Physics*, 136(19):194109, 2012.

[59] Chengteh Lee, Weitao Yang, and Robert G. Parr. Development of the Colle-Salvetti Correlation-Energy Formula into a Functional of the Electron Density. *Physical Review B*, 37:785–789, Jan 1988.

[60] Patrick J. Lestrange, David B. Williams-Young, Alessio Petrone, Carlos A. Jimenez-Hoyos, and Xiaosong Li. An Efficient Implementation of Variation After Projection Generalized Hartree-Fock. *Journal of Chemical Theory and Computation*, 14:588–596, 2018.

[61] Ingo H. Leubner and Joe E. Hodgkins. Temperature Dependence of the Phosphorescence Lifetime of Benzene and N-Alkylbenzenes Between 4.2 and 100.deg.K. *The Journal of Physical Chemistry*, 73(8):2545–2550, 1969.

[62] Zhendong Li, Yunlong Xiao, and Wenjian Liu. On the Spin Separation of Algebraic Two-Component Relativistic Hamiltonians. *Journal of Chemical Physics*, 137:154114, 2012.

[63] Junzi Liu and Lan Cheng. An Atomic Mean-Field Spin-Orbit Approach within Exact Two-Component Theory for a Non-Perturbative Treatment of Spin-Orbit Coupling. *Journal of Chemical Physics*, 148(14):144108, 2018.

[64] Wenjian Liu. Ideas of Relativistic Quantum Chemistry. *Molecular Physics*, 108:1679–1706, 2010.

[65] Wenjian Liu. *Handbook of Relativistic Quantum Chemistry*. Springer-Verlag Berlin Heidelberg, 2017.

[66] Wenjian Liu and Daoling Peng. Infinite-Order Quasirelativistic Density Functional Method Based on the Exact Matrix Quasirelativistic Theory. *Journal of Chemical Physics*, 125:044102, 2006.

[67] Wenjian Liu and Daoling Peng. Exact Two-component Hamiltonians Revisited. *Journal of Chemical Physics*, 131(3):031104, 2009.

[68] Wenjian Liu and Yunlong Xiao. Relativistic Time-Dependent Density Functional Theories. *Chemical Society Reviews*, 47:4481–4509, 2018.

[69] Eleonora Luppi and Martin Head-Gordon. Computation of High-Harmonic Generation Spectra of H_2 and N_2 in Intense Laser Pulses using Quantum Chemistry Methods and Time-Dependent Density Functional Theory. *Molecular Physics*, 110(9-10):909–923, 2012.

[70] Christel M. Marian. Spin-Orbit Coupling and Intersystem Crossing in Molecules. *WIREs Computational Molecular Science*, 2(2):187–203, mar 2012.

[71] Donald Allan McQuarrie. *Statistical Mechanics*. Harper's Chemistry Series. Harper-Collins Publishing, Inc., New York, 1976.

[72] Boris F. Minaev and Hans Ãgren. Spin-catalysis phenomena. *International Journal of Quantum Chemistry*, 57(3):519–532, 1996.

[73] Hendrik J. Monkhorst. Calculation of Properties With the Coupled-Cluster Method. *International Journal of Quantum Chemistry*, 12:421–432, 1977.

[74] Philip M. Morse. Diatomic Molecules According to the Wave Mechanics. II. Vibrational Levels. *Physical Review*, 34:57–64, Jul 1929.

[75] Debashis Mukherjee and Paresh K. Mukherjee. A Response-Function Approach to the Direct Calculation of the Transition-Energy in a Multiple-Cluster Expansion Formalism. *Chemical Physics*, 39(3):325 – 335, 1979.

[76] Hiroshi Nakatsuji, K. Ohta, and Kimihiko Hirao. Cluster Expansion of the Wave Function. Electron Correlations in the Ground State, Valence and Rydberg Excited States, Ionized States, and Electron Attached States of Formaldehyde by SAC and SAC-CI Theories. *Journal of Chemical Physics*, 75:2952–2958, 1981.

[77] Daniel R. Nascimento and A. Eugene DePrince. Linear Absorption Spectra from Explicitly Time-Dependent Equation-of-Motion Coupled-Cluster Theory. *Journal of Chemical Theory and Computation*, 12:5834–5840, 2016.

[78] Daniel R. Nascimento and A. Eugene DePrince. Simulation of Near-Edge X-ray Absorption Fine Structure with Time-Dependent Equation-of-Motion Coupled-Cluster Theory. *Journal of Physical Chemistry Letters*, 8:2951–2957, 2017.

[79] Patrick Norman and Andreas Dreuw. Simulating X-ray Spectroscopies and Calculating Core-Excited States of Molecules. *Chemical Reviews*, 118(15):7208–7248, 2018. PMID: 29894157.

[80] Takeshi Noro, Masahiro Sekiya, and Toshikatsu Koga. Segmented contracted basis sets for atoms H through Xe: Sapporo-(DK)-nZP sets (n = D, T, Q). *Theoretical Chemistry Accounts*, 131:1124, 2012.

[81] Takeshi Noro, Masahiro Sekiya, and Toshikatsu Koga. Segmented Contracted Basis Sets for Atoms H Through Xe: Sapporo-(DK)-nZP Sets (n = D, T, Q). *Theoretical Chemistry Accounts*, 131(2):1124, Feb 2012.

[82] Himadri Pathak, Sudip Sasmal, Malaya K. Nayak, Nayana Vaval, and Sourav Pal. Relativistic Equation-of-motion Coupled-Cluster Method for the Electron Attachment Problem. *Computational and Theoretical Chemistry*, 1076:94 – 100, 2016.

[83] Thomas Bondo Pedersen and Simen Kvaal. Symplectic Integration and Physical Interpretation of Time-Dependent Coupled-Cluster Theory. *Journal of Chemical Physics*, 150(14):144106, 2019.

[84] Bo Peng, Patrick J Lestrange, Joshua J Goings, Marco Caricato, and Xiaosong Li. Energy-Specific Equation-of-Motion Coupled-Cluster Methods for High-Energy Excited States: Application to K-Edge X-Ray Absorption Spectroscopy. *Journal of Chemical Theory and Computation*, 11(9):4146–4153, 2015.

[85] Daoling Peng, Wenjian Liu, Yunlong Xiao, and Lan Cheng. Making Four- and Two-Component Relativistic Density Functional Methods Fully Equivalent Based on the Idea of From Atoms to Molecule. *Journal of Chemical Physics*, 127:104106, 2007.

[86] Daoling Peng, Nils Middendorf, Florian Weigend, and Markus Reiher. An Efficient Implementation of Two-Component Relativistic Exact-Decoupling Methods for Large Molecules. *Journal of Chemical Physics*, 138:184105, 2013.

[87] D.S. Pesic and S. Weniger. Analyse Etude de la Structure de Vibration du Systeme B-X de la Molecule $^{63}Cu^{65}Cu$. *Comptes rendus de l'Académie des Sciences B*, 272:46, 1971.

[88] D.S. Pesic and S. Weniger. Analyse Rotationnelle des Bandes du Systme A-X de $^{63}Cu_2$. *Comptes rendus de l'Académie des Sciences B*, 273:602, 1971.

[89] Alessio Petrone, David B. Williams-Young, Shichao Sun, Torin F. Stetina, and Xiaosong Li. An efficient implementation of two-component relativistic density functional theory with torque-free auxiliary variables. *European Physical Journal B*, 91(7):169, 2018.

[90] Lucjan Piela. Appendix S - Population Analysis. In Lucjan Piela, editor, *Ideas of Quantum Chemistry (Second Edition)*, pages e143–e147. Elsevier, Oxford, second edition edition, 2014.

[91] Benjamin P. Pritchard, Doaa Altarawy, Brett Didier, Tara D. Gibsom, and Theresa L. Windus. A New Basis Set Exchange: An Open, Up-to-Date Resource for the Molecular Sciences Community. *Journal of Chemical Information and Modeling*, 59:4814–4820, 2019.

[92] Pekka Pyykkö. Relativistic Effects in Structural Chemistry. *Chemical Reviews*, 88(3):563–594, 1988.

[93] Pekka Pyykkö. Relativistic Effects in Chemistry: More Common Than You Thought. *Annual Review of Physical Chemistry*, 63(1):45–64, 2012.

[94] T.V. Ramakrishna Rao and S.V.J. Lakshman. RKRV Curves, R-Centroids and Franck-Condon Factors for Bands of the $^{63}Cu_2$ Molecule. *Journal of Quantitative Spectroscopy and Radiative Transfer*, 11(7):1157–1161, 1971.

[95] Vitaly A. Rassolov, Mark A. Ratner, John A. Pople, Paul C. Redfern, and Larry A. Curtiss. 6-31G* Basis Set for Third-Row Atoms. *Journal of Computational Chemistry*, 22, 2001.

[96] Markus Reiher and Alexander Wolf. *Relativistic Quantum Chemistry.* Wiley-VCH, second edition, 2015.

[97] Björn O. Roos, Roland Lindh, Per-Åke Malmqvist, Valera Veryazov, and Per-Olof Widmark. Main Group Atoms and Dimers Studied with a New Relativistic ANO Basis Set. *Journal of Physical Chemistry A*, 108:2851–2858, 2004.

[98] Björn O. Roos, Roland Lindh, Per-Åke Malmqvist, Valera Veryazov, and Per-Olof Widmark. New Relativistic ANO Basis Sets for Transition Metal Atoms. *Journal of Physical Chemistry A*, 109:6575–6579, 2005.

[99] Jean Ruamps. Spectre D'Emission des Molecules Cu_2, Ag_2, et Au_2. *Comptes Rendus*, 238:1489, 1954.

[100] Jean Ruamps. Production et Étude du Spectre Optique de Molécules Diatomiques de Métaux et Contribution au Calcul Théorique des Intensités. *Annales de Physique*, 13(4):1111–1157, 1959.

[101] Takeshi Sato, Himadri Pathak, Yuki Orimo, and Kenichi L. Ishikawa. Communication: Time-Dependent Optimized Coupled-Cluster Method for Multielectron Dynamics. *Journal of Chemical Physics*, 148(5):051101, 2018.

[102] Trond Saue. Relativistic Hamiltonians for Chemistry: A Primer. *ChemPhysChem*, 12:3077–3094, 2011.

[103] Paul Schissel. Dissociation Energies of Cu_2, Ag_2, and Au_2. *Journal of Chemical Physics*, 26(5):1276–1280, 2004.

[104] K. Schönhammer and O. Gunnarsson. Time-Dependent Approach to the Calculation of Spectral Functions. *Physical Review B*, 18:6606–6614, Dec 1978.

[105] Karen L. Schuchardt, Brett T. Didier, Todd Elsethagen, Lisong Sun, Vidhya Gurumoorthi, Jared Chase, Jun Li, and Theresa L. Windus. Basis Set Exchange: A Community Database for Computational Sciences. *Journal of Chemical Information and Modeling*, 47:1045–1052, 2007.

[106] Isaiah Shavitt and Rodney J. Bartlett. *Many-Body Methods in Chemistry and Physics.* MBPT and Coupled-Cluster Theory. Cambridge University Press, August 2009.

[107] Avijit Shee, Trond Saue, Lucas Visscher, and André Severo Pereira Gomes. Equation-of-Motion Coupled-Cluster Theory Based on the 4-Component Dirac–Coulomb(–Gaunt) Hamiltonian. Energies for Single Electron Detachment, Attachment, and Electronically Excited States. *Journal of Chemical Physics*, 149(17):174113, 2018.

[108] S. Smoes, F. Mandy, A. Vander Auwera-Mahieu, and J. Drowart. Determination by the Mass Spectrometric Knudsen Cell Method of the Dissociation Energies of the Group IB Chalcogenides. *Bulletin des Sociétés Chimiques Belges*, 81(1):45–56, 1972.

[109] Jason A Sonk, Marco Caricato, and H Bernhard Schlegel. TD-CI Simulation of the Electronic Optical Response of Molecules in Intense Fields: Comparison of RPA, CIS, CIS(D), and EOM-CCSD. *Journal of Physical Chemistry A*, 115(18):4678–4690, 2011.

[110] John F. Stanton and Rodney J. Bartlett. The Equation of Motion Coupled-Cluster Method. A Systematic Biorthogonal Approach to Molecular Excitation Energies, Transition Probabilities, and Excited State Properties. *Journal of Chemical Physics*, 98(9):7029–7039, 1993.

[111] John F. Stanton, Jürgen Gauss, John D. Watts, and Rodney J. Bartlett. A Direct Product Decomposition Approach for Symmetry Exploitation in Many-Body Methods. I. Energy Calculations. *Journal of Chemical Physics*, 94:4334–4345, 1991.

[112] Torin F. Stetina, Joseph M. Kasper, and Xiaosong Li. Modeling $L_{2,3}$-Edge X-ray Absorption Spectroscopy with Linear Response Exact Two-Component Relativistic Time-Dependent Density Functional Theory. *Journal of Chemical Physics*, 150:234103, 2019.

[113] Casey Sugie, Alexandra Navrotsky, Stefan Lauterbach, Hans-Joachim Kleebe, and Gabriela Mera. Structure and Thermodynamics of Silicon Oxycarbide Polymer-Derived Ceramics with and without Mixed-Bonding. *Materials*, 14(15), 2021.

[114] Kazuyoshi Sushida, Masahisa Fujita, Takeshi Takemura, and Hiroaki Baba. Phosphorescence from Pyridine Vapor. *Journal of Chemical Physics*, 78(1):588–589, 01 1983.

[115] Kazuyoshi Sushida, Masahisa Fujita, Takeshi Takemura, and Hiroaki Baba. Phosphorescence and its Characteristics in Pyridine Vapor. *Chemical Physics*, 88(2):221–228, 1984.

[116] Douglas G. J. Sutherland, Masoud Kasrai, G. M. Bancroft, Z. F. Liu, and Kim H. Tan. Si L- and K-Edge X-Ray-Absorption Near-Edge Spectroscopy of Gas-Phase $Si(CH_3)_x(OCH_3)_{4-x}$: Models for Solid-State Analogs. *Phys. Rev. B*, 48:14989–15001, Nov 1993.

[117] Zheyan Tu, Fan Wang, and Xiangyuan Li. Equation-of-motion Coupled-Cluster

Method for Ionized States with Spin-Orbit Coupling. *Journal of Chemical Physics*, 136(17):174102, 2012.

[118] Samat Tussupbayev, Niranjan Govind, Kenneth Lopata, and Christopher J. Cramer. Comparison of Real-Time and Linear-Response Time-Dependent Density Functional Theories for Molecular Chromophores Ranging from Sparse to High Densities of States. *Journal of Chemical Theory and Computation*, 11(3):1102–1109, 2015.

[119] Andrew J. S. Valentine and Xiaosong Li. Toward the Evaluation of Intersystem Crossing Rates with Variational Relativistic Methods. *Journal of Chemical Physics*, 151:084107, 2019.

[120] Eugene Vecharynski, Chao Yang, and Fei Xue. Generalized Preconditioned Locally Harmonic Residual Method for Non-Hermitian Eigenproblems. *SIAM Journal on Scientific Computing*, 38:A500–A527, 2016.

[121] Valera Veryazov, Per-Olof Widmark, and Björn O. Roos. Relativistic Atomic Natural Orbital Type Basis Sets for the Alkaline and Alkaline-Earth Atoms Applied to the Ground-State Potentials for the Corresponding Dimers. *Theoretical Chemistry Accounts*, 111:345–351, 2004.

[122] Zhifan Wang, Zheyan Tu, and Fan Wang. Equation-of-Motion Coupled-Cluster Theory for Excitation Energies of Closed-Shell Systems With Spin-Orbit Coupling. *Journal of Chemical Theory and Computation*, 10:5567–5576, 2014.

[123] Horst Weiss, Reinhart Ahlrichs, and Marco Häser. A Direct Algorithm for Self-Consistent-Field Linear Response Theory and Application to C_{60}: Excitation Energies, Oscillator Strengths, and Frequency-Dependent Polarizabilities. *Journal of Chemical Physics*, 99(2):1262–1270, 1993.

[124] David Williams-Young, Franco Egidi, and Xiaosong Li. Relativistic Two-Component

Particle-Particle Tamm-Dancoff Approximation. *Journal of Chemical Theory and Computation*, 12(11):5379–5384, 2016.

[125] David B Williams-Young, Alessio Petrone, Shichao Sun, Torin F Stetina, Patrick Lestrange, Chad E Hoyer, Daniel R Nascimento, Lauren Koulias, Andrew Wildman, Joseph Kasper, Joshua J. Goings, Feizhi Ding, A. Eugene DePrince III, Edward F. Valeev, and Xiaosong Li. The Chronus Quantum (ChronusQ) Software Package. *WIREs Computational Molecular Science*, 2019.

[126] David B Williams-Young, Alessio Petrone, Shichao Sun, Torin F Stetina, Patrick Lestrange, Chad E Hoyer, Daniel R Nascimento, Lauren Koulias, Andrew Wildman, Joseph Kasper, Joshua J. Goings, Feizhi Ding, A. Eugene DePrince III, Edward F. Valeev, and Xiaosong Li. The Chronus Quantum (ChronusQ) Software Package. *WIREs Computational Molecular Science*, 10:e1436, 2020.

[127] Dong-Dong Yang, Fan Wang, and Jingwei Guo. Equation of Motion Coupled Cluster Method for Electron Attached States with Spin–Orbit Coupling. *Chemical Physics Letters*, 531:236 – 241, 2012.

[128] Stephen H. Yuwono, Brandon C. Cooper, Tianyuan Zhang, Xiaosong Li, and III DePrince, A. Eugene. Time-dependent equation-of-motion coupled-cluster simulations with a defective Hamiltonian. *Journal of Chemical Physics*, 159(4):044113, 2023.

[129] Patric Zimmermann, Sergey Peredkov, Paula Macarena Abdala, Serena DeBeer, Moniek Tromp, Christoph Maceller, and Jeroen A. van Bokhoven. Modern X-Ray Spectroscopy: XAS and XES in the Laboratory. *Coordination Chemistry Reviews*, 423:213466, 2020.